










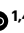



Dietary- and host-derived metabolites are used by diverse gut bacteria for anaerobic respiration

Received: 11 January 2023

Accepted: 14 November 2023

Published online: 4 January 2024

 Check for updates

Alexander S. Little^{1,2}, Isaac T. Younker ^{1,2}, Matthew S. Schechter ^{1,2}, Paola Nol Bernardino^{1,2}, Raphaël Méheust ³, Joshua Stemczynski^{1,2}, Kaylie Scorza^{1,2}, Michael W. Mullowney ¹, Deepti Sharan ^{1,2}, Emily Waligurski ¹, Rita Smith ¹, Ramanujam Ramanswamy ¹, William Leiter ¹, David Moran¹, Mary McMillin¹, Matthew A. Odenwald ^{1,4}, Anthony T. Iavarone⁵, Ashley M. Sidebottom¹, Anitha Sundararajan¹, Eric G. Pamer ^{1,2,6}, A. Murat Eren ^{7,8} & Samuel H. Light ^{1,2} 

Respiratory reductases enable microorganisms to use molecules present in anaerobic ecosystems as energy-generating respiratory electron acceptors. Here we identify three taxonomically distinct families of human gut bacteria (Burkholderiaceae, Eggerthellaceae and Erysipelotrichaceae) that encode large arsenals of tens to hundreds of respiratory-like reductases per genome. Screening species from each family (*Sutterella wadsworthensis*, *Eggerthella lenta* and *Holdemania filiformis*), we discover 22 metabolites used as respiratory electron acceptors in a species-specific manner. Identified reactions transform multiple classes of dietary- and host-derived metabolites, including bioactive molecules resveratrol and itaconate. Products of identified respiratory metabolisms highlight poorly characterized compounds, such as the itaconate-derived 2-methylsuccinate. Reductase substrate profiling defines enzyme–substrate pairs and reveals a complex picture of reductase evolution, providing evidence that reductases with specificities for related cinnamate substrates independently emerged at least four times. These studies thus establish an exceptionally versatile form of anaerobic respiration that directly links microbial energy metabolism to the gut metabolome.

Heterotrophic cellular respiration is defined by the oxidation of an electron donor and the passage of resulting electrons through an electron transport chain to a terminal electron acceptor¹. Electron transfer is coupled to the creation of an ion gradient that, in turn, powers oxidative adenosine triphosphate (ATP) synthesis through ATP synthase¹. While

molecular oxygen is a hallmark respiratory electron acceptor, microorganisms residing in oxygen-poor environments possess respiratory metabolisms that use alternative electron acceptors¹.

Fermentative metabolisms dominate the anaerobic gut microbial ecosystem, but several classical respiratory metabolisms have

¹Duchossois Family Institute, University of Chicago, Chicago, IL, USA. ²Department of Microbiology, University of Chicago, Chicago, IL, USA. ³Génomique Métabolique, CEA, Genoscope, Institut François Jacob, Université d'Évry, Université Paris-Saclay, CNRS, Evry, France. ⁴Section of Gastroenterology, Hepatology, and Nutrition, Department of Medicine, University of Chicago, Chicago, IL, USA. ⁵QB3/Chemistry Mass Spectrometry Facility, University of California, Berkeley, Berkeley, CA, USA. ⁶Section of Infectious Diseases & Global Health, Department of Medicine, University of Chicago, Chicago, IL, USA. ⁷Helmholtz Institute for Functional Marine Biodiversity, Oldenburg, Germany. ⁸Institute for Chemistry and Biology of the Marine Environment, University of Oldenburg, Oldenburg, Germany. ✉e-mail: samlight@uchicago.edu

been identified. Diverse sulfate-reducing bacteria use different sulfate respiratory electron acceptors². Clostridial acetogens and archaeal methanogens respire carbon dioxide³. Bacteroidales convert fermentative substrates to the electron acceptor fumarate, which is reduced by the enzyme fumarate reductase⁴. Various other gut bacteria convert exogenous four-carbon dicarboxylates, including the amino acid aspartate, to fumarate, which is similarly respired⁵. In the inflamed gut, electron acceptors generated by immune cells (hydrogen peroxide, tetrathionate and nitrate) fuel respiratory growth of pathogenic and commensal Enterobacteriaceae^{6–8}.

While most identified respiratory gut metabolisms use inorganic electron acceptors, two observations suggest that other types of respiratory electron acceptors may be underappreciated. First, a recent study found that *Eggerthella lenta* used the neurotransmitter dopamine as a respiratory electron acceptor and identified several related catechols that were similarly reductively dehydroxylated⁹. Second, a bioinformatic survey found that multiple Eggerthellaceae family bacteria encode many enzymes homologous to the respiratory dimethylsulfoxide (DMSO) reductase and noted that they might enable the use of different electron acceptors¹⁰. These observations underscore the possibility that gut microorganisms possess the capacity to use a large and chemically diverse collection of respiratory electron acceptors.

In this Article, we use a genome-mining-based approach to interrogate respiratory electron acceptor usage in the human gut microbiome. We find that three taxonomically distinct families of gut microorganisms encode exceptionally large numbers of respiratory-like reductases. We show that representative species from each clade exhibit respiratory activities and identify diverse small-molecule electron acceptors used in a strain-dependent manner. In addition, we pair specific reductases with their substrates to reveal a convoluted relationship between reductase sequence and substrate specificity. By probing reductases with distinct active-site architectures, we show that parallel evolutionary trajectories generated reductases that achieve similar activities through distinct mechanisms. These studies establish a distinctive mode of bacterial respiration, defined by the versatile use of organic electron acceptors, and contextualize the role of energy metabolism in shaping the gut metabolome.

Results

Distantly related bacteria encode large reductase arsenals

Previous studies have identified a number of microbial respiratory reductases that enable the use of distinct electron acceptors. Many of these reductases are evolutionarily related and placed within one of two enzyme superfamilies by hidden Markov models (HMMs). Members of the ‘molybdopterin’ superfamily (HMM PF00384)—exemplified by DMSO reductase—contain a catalytic domain that binds the redox-active cofactor molybdopterin and tend to act on inorganic respiratory electron acceptors (Fig. 1a and Supplementary Table 1)^{9,11–22}. Members of the ‘flavin’ superfamily (HMM PF00890)—exemplified by fumarate and urocanate reductases—contain a catalytic domain that binds the redox-active cofactor flavin adenine dinucleotide and tend to act on organic respiratory electron acceptors (Fig. 1b and Supplementary Table 1)^{23–28}. Structural and biochemical studies of enzymes within the molybdopterin and flavin superfamilies suggest that each contains a broadly conserved electron transfer mechanism but active-site distinctions that confer different substrate specificities and activities^{29,30}.

Most characterized respiratory reductases are soluble proteins that receive electrons from the electron transport chain in the cytosolic membrane. While respiratory reductases can be associated with either the cytosolic or the extracytosolic side of the cytosolic membrane, we observed that most characterized flavin and molybdopterin respiratory reductases contain an N-terminal signal peptide characteristic of extracytosolic localization (Supplementary Table 1). By contrast, most molybdopterin and flavin superfamily enzymes that possess an obvious

non-respiratory reductase functionality are cytosolically localized and lack an N-terminal signal peptide (Supplementary Table 1).

Based on the role of established flavin and molybdopterin reductases in respiratory electron acceptor usage, we reasoned that a survey of genes predicted to encode secreted flavin or molybdopterin superfamily members could facilitate the identification of respiratory gut microorganisms. We analysed 1,533 genomes and metagenome-assembled genomes from a recently compiled collection of diverse human gut prokaryotes and observed a striking distribution in the number of reductases per genome³¹. While most genomes encode less than 5 reductases, we identified a small subset of ‘high reductase’ genomes that encode more than 30 (and as many as 103) reductases (Fig. 1c and Supplementary Table 2). Consistent with identified reductases having an extracellular localization and respiratory functionality, most contained a predicted N-terminal signal peptide (Supplementary Table 2).

Further taxonomic analyses revealed that ‘high reductase’ genomes form three distinct clades that span multiple genera in the (1) Actinobacteria family Eggerthellaceae, (2) Firmicutes family Erysipelotrichaceae and (3) Proteobacteria family Burkholderiaceae (Fig. 1d). Notably, species from each clade—including *E. lenta* from Eggerthellaceae, *Sutterella wadsworthensis* from Burkholderiaceae and *Holdemania filiformis* from Erysipelotrichaceae—are prevalent, low- to moderate-abundance members of the human gut microbiome³². Expanding the analyses to include bacteria found outside the human gut revealed that high-reductase clades include bacteria with >200 reductases per genome and exhibit complex reductase gain-and-loss patterns indicative of a convoluted evolutionary history (Extended Data Fig. 1, Supplementary Table 3 and Supplementary Discussion). These analyses thus define three taxonomically distinct groups of gut bacteria that encode large numbers of respiratory-like reductases.

Reductase-encoding bacteria exhibit respiratory growth

To test whether gut microorganisms with a high number of reductases per genome possessed respiratory capabilities, we selected *E. lenta*, *S. wadsworthensis* and *H. filiformis* strains for experimental characterization. We identified a flavin reductase with >50% sequence identity to a previously characterized respiratory urocanate reductase (UrdA) encoded within each strain’s genome, suggesting that the small-molecule urocanate provided a suitable candidate for preliminary investigations of respiratory growth^{24,25}.

As use of a respiratory electron acceptor is conditional upon oxidation of an electron donor, we screened common respiratory electron donors for the ability to induce urocanate-dependent growth enhancement. We observed a synergistic growth enhancement of *E. lenta* and *S. wadsworthensis*, establishing formate as a viable electron donor for these strains (Fig. 2a). *H. filiformis* also exhibited enhanced growth in the presence of urocanate, but requirements for a rich growth medium hindered identification of a respiratory electron donor (Fig. 2a). Consistent with the observed phenotypes reflecting respiratory activity, growth enhancement of each strain tracked with urocanate reduction to imidazole propionate and depended upon the electron-accepting properties of urocanate (that is, the reduced reaction product did not enhance growth; Fig. 2a–c). Further supporting the role of respiration in these growth phenotypes, we found that urocanate stimulated ATP synthesis of all three strains (Fig. 2d). These results thus show that *E. lenta*, *S. wadsworthensis* and *H. filiformis* possess respiratory metabolic capabilities and similarly use urocanate as a respiratory electron acceptor.

Reductase-encoding bacteria use diverse electron acceptors

Having established the respiratory capabilities of our strains, we hypothesized that their large number of reductases reflected an extreme versatility in respiratory electron acceptor utilization capabilities. As most reductases encoded by these strains were distantly

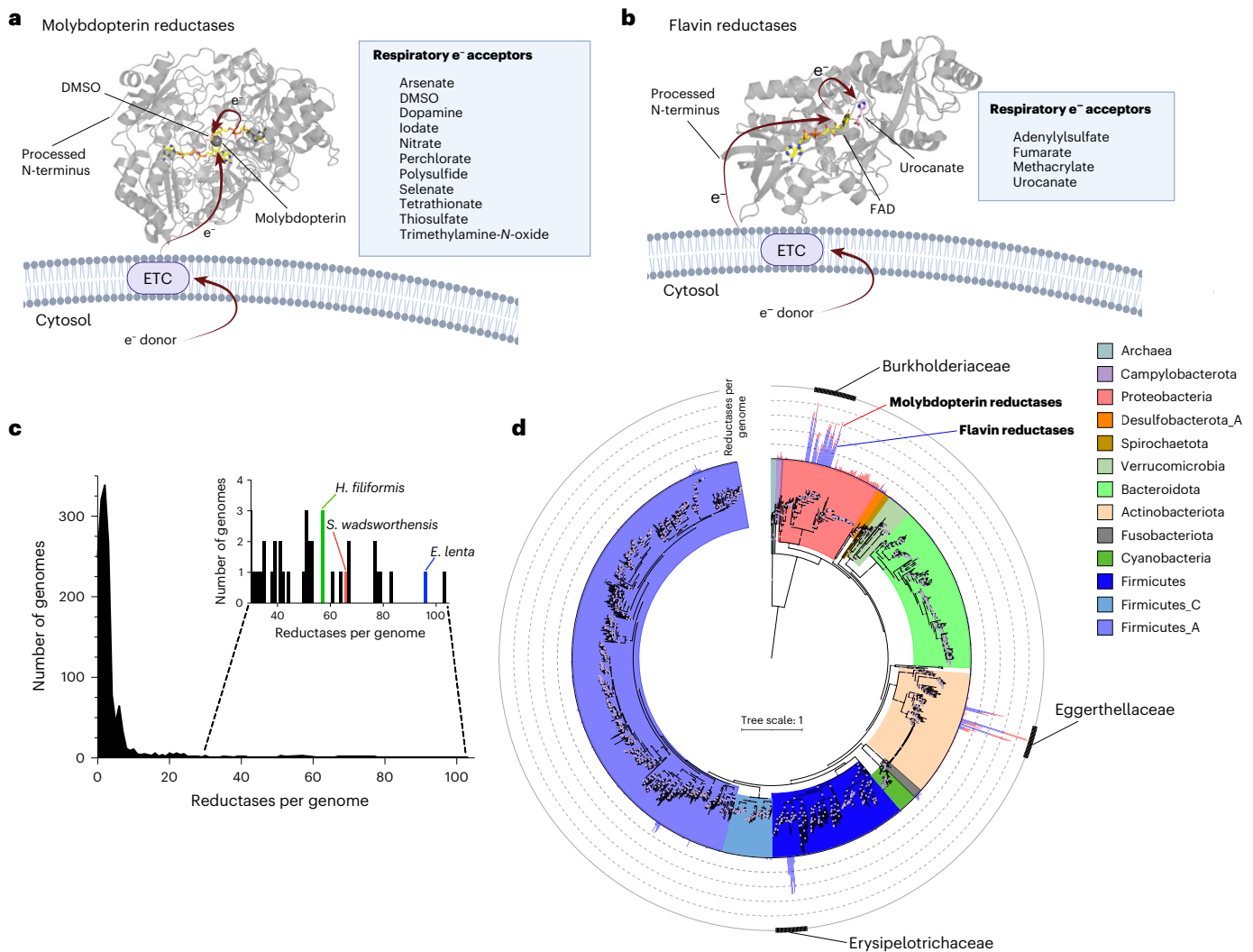


Fig. 1 | Respiratory reductase orthologues are highly over-represented in three distinct lineages of gut bacteria. **a**, General mechanism and electron acceptors used by different previously characterized respiratory molybdopterin reductases (Pfam PF00384). Arrows highlight the electron (e^-) transfer path from the electron transport chain (ETC) to DMSO in the DMSO reductase crystal structure (PDB code 4DMR). **b**, General mechanism and electron acceptors used by previously characterized respiratory flavin reductases (Pfam PF00890). Arrows highlight electron transfer to substrate in the *S. oneidensis* urocanate reductase co-complex crystal structure (PDB code 6T87). **c**, Distribution of the

number of flavin and molybdopterin reductases in 1,533 representative human gut bacteria genomes and metagenome-assembled genomes. **d**, Phylogenetic reconstruction of the evolutionary history of genomes analysed in **c**. The maximum likelihood tree was constructed based on a concatenated alignment of 14 ribosomal proteins under an LG + I + G4 model of evolution (2,092 amino acid sites). The number of flavin (blue) and molybdopterin (red) reductases with a computationally predicted signal peptide in each genome are plotted on the outer ring of the tree.

related to functionally characterized enzymes and thus lacked obvious substrates, we assembled a panel of metabolites that possessed electron-accepting properties and could be present in the gastrointestinal tract.

By screening *E. lenta*, *S. wadsworthensis* and *H. filiformis* strains, we identified 19 compounds that supported growth of at least 1 species (Fig. 3a and Extended Data Figs. 2–4). For most identified compounds, we confirmed that (1) their depletion coincided with the accumulation of a reduced product, (2) this reduced product did not impact growth and (3) the presence of an electron donor was required for growth enhancement (Extended Data Figs. 2–4). Through complementary enzymatic activity assays, we identified three additional molecules (resveratrol, catechin and epicatechin) that were used as electron acceptors but, due to poor solubility or other factors, were not associated with enhanced growth under the tested conditions (Fig. 3b,c and Extended Data Fig. 5). Further corroborating the respiratory role of

observed activities, we confirmed that the representatives of each class of identified electron acceptors promoted ATP production (Extended Data Fig. 6).

Identified electron acceptors included multiple cinnamates, flavonoids, four-carbon dicarboxylates, sulfoxides with electron-accepting groups including carbon–oxygen bonds, hydroxyls, sulfoxides and alkenes (Fig. 3a–c). Different substrate classes exhibited species-specific patterns of utilization (further explored in Supplementary Discussion, Extended Data Figs. 2–7). In addition to these broader substrate classes, we found that (1) *E. lenta* and *S. wadsworthensis* reduced an enoate group in shikimate, an intermediate in the biosynthesis of aromatic compounds (Fig. 3a–c, and Extended Data Figs. 2 and 3); (2) *E. lenta* and *H. filiformis* reduced an alkene group in resveratrol, a plant phenylpropanoid present in different foods and beverages, that has many reported effects on mammalian physiology (Extended Data Fig. 5); and (3) *E. lenta* reduced an alkene group in itaconate, a mammalian immune

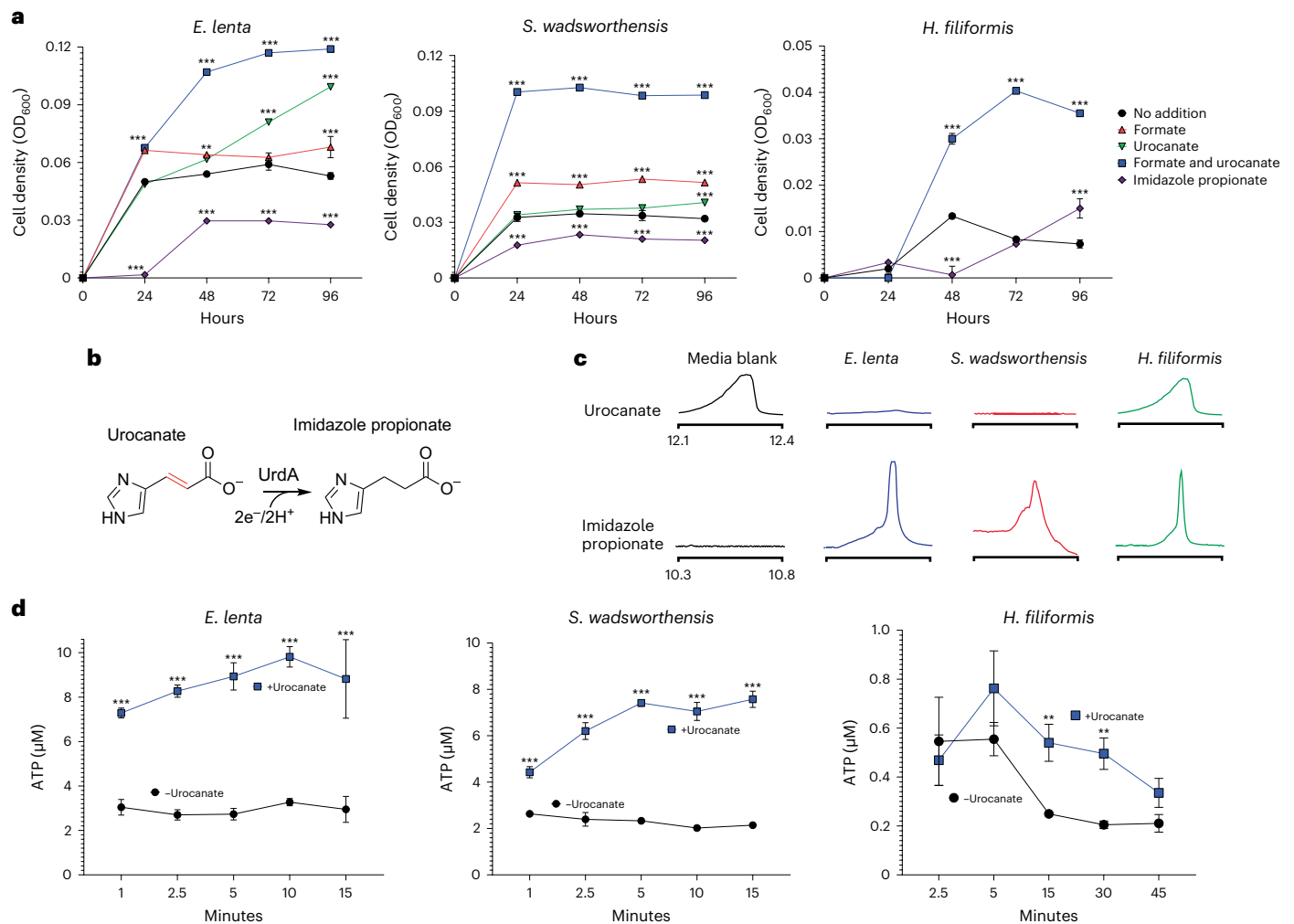


Fig. 2 | 'High reductase' gut bacteria exhibit respiratory growth properties.

a, Growth of *E. lenta* DSM2243, *S. wadsworthensis* DFI.4.78 and *H. filiformis* DSM12042 strains in the presence of electron donor (formate), electron acceptor (urocanate) and product of urocanate reduction (imidazole propionate). **b**, Reaction catalyzed by urocanate reductase UrdA. **c**, GC-MS extracted ion

chromatograms in formate-urocanate-supplemented culture supernatants following cultivation of the indicated strains. **d**, ATP produced by cells suspended in formate-supplemented buffer. For **a**, data are mean \pm s.d. ($n = 3$ independent biological replicates); for **d**, data are mean \pm s.d. ($n = 3$ technical replicates). ** $P < 0.01$; *** $P < 0.001$. Two-way ANOVA, multiple test versus media alone.

signalling molecule (Fig. 3c and Extended Data Fig. 2)^{33–35}. Collectively, these results define a complex species-dependent pattern of electron acceptor usage.

Reductase substrates and products are present in faeces

To clarify the relevance of identified electron acceptors within the gut microbiome, we measured faecal metabolites from a population of 19 non-antibiotic-treated healthy donors and 22 hospitalized antibiotic-treated patients with severely diminished microbiome complexity (Extended Data Fig. 8a). As the multiple differences that distinguish these healthy and antibiotic-treated groups preclude the definitive attribution of metabolite differences to the microbiome, we additionally sought a more controlled experimental system. We thus measured electron acceptors and their reduced products in mouse faecal samples before and after treatment with a cocktail of broad-spectrum antibiotics that severely disrupted the gut microbiome (Extended Data Fig. 8b).

Distinct compounds were detected in the mouse and human samples but, in both populations, levels of reductase substrates and products trended lower in the antibiotic-treated groups (Fig. 3d,e and Supplementary Tables 4 and 5). This pattern was evident for multiple

cinnamates, which can be produced from bacterial breakdown of larger dietary polyphenols, urocanate and shikimate, which are intermediates in bacterial metabolic pathways and, perhaps most strikingly, for the immunometabolite itaconate (Fig. 3d and Supplementary Table 4). Itaconate and its reduced product 2-methylsuccinate were detected in virtually every healthy human faecal sample but were below the limit of detection for most samples from the antibiotic-treated group (Fig. 3d and Supplementary Table 4). These studies establish that the identified respiratory electron acceptors are present within the mammalian gastrointestinal tract and responsive to the gut microbiome.

Respiratory electron acceptors selectively induce reductases

An examination of the genomic context of *E. lenta*, *S. wadsworthensis* and *H. filiformis* flavin and molybdopterin reductase genes revealed that they frequently colocalized with putative transcriptional regulators, although notable species-specific differences in the type of regulators were evident. *S. wadsworthensis* and *H. filiformis* reductase genes often colocalized with histidine kinase two-component systems or typical helix-turn-helix (HTH) cytosolic transcriptional regulators, whereas 64 *E. lenta* reductase genes directly neighbour a recently described family of transmembrane transcriptional regulators (Fig. 4a,b and

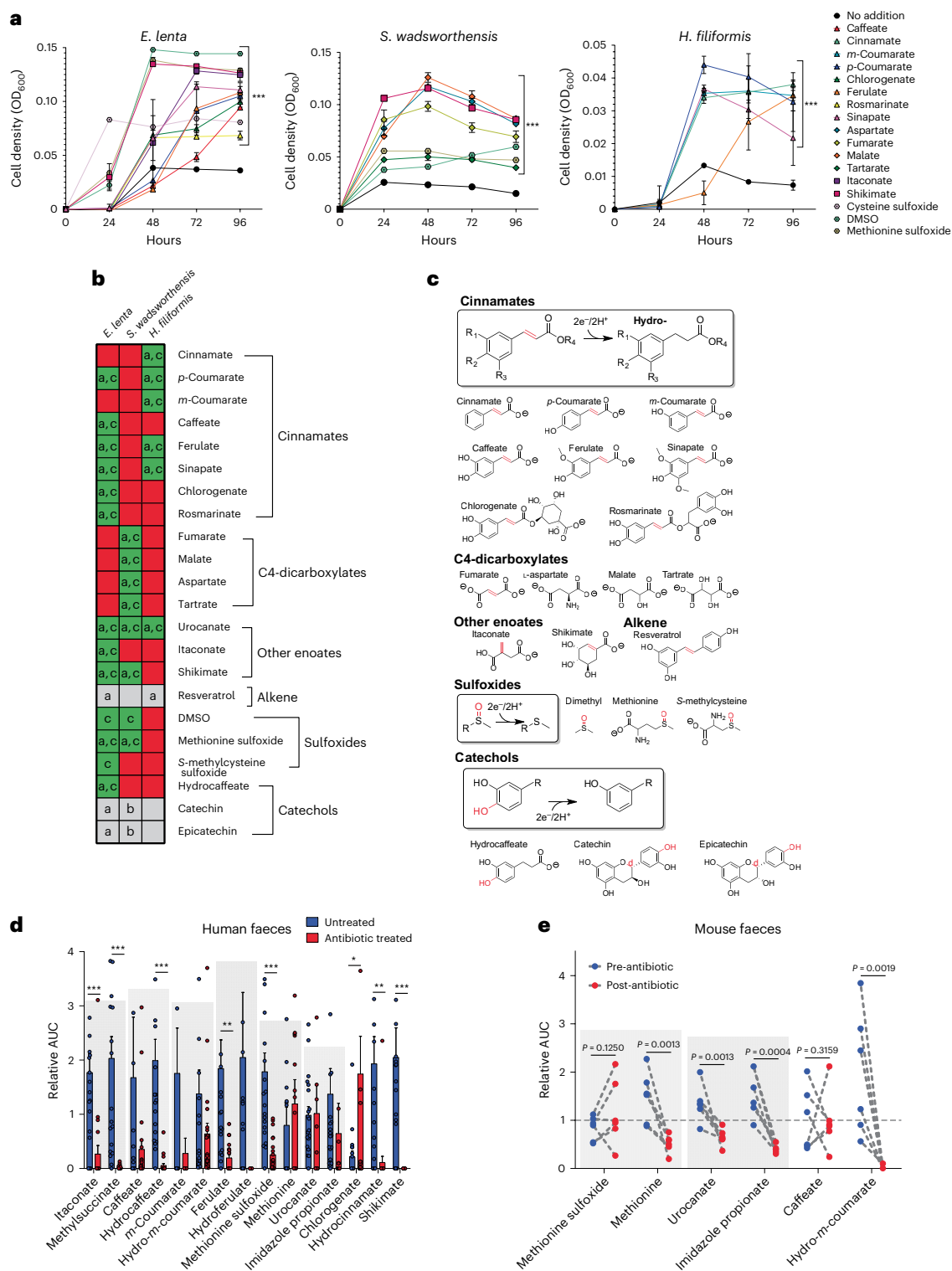


Fig. 3 | 'High reductase' gut bacteria use diverse respiratory electron acceptors. **a**, *E. lenta* DSM2243, *S. wadsworthensis* DFI.4.78 and *H. filiformis* DFI.9.20 growth in media supplemented with formate and identified growth-stimulating small molecules. **b**, Summary of electron acceptor usage findings. Green indicates growth enhancement, red indicates no enhancement and grey indicates not tested. Letters indicate whether: (a) a reduced product was detected after growth, (b) partial product detected, and (c) experimentally confirmed respiratory-like phenotype. **c**, Summary of identified reductase activities. The electron-accepting bond is highlighted in red. Site of benzylic C–O cleavage (d). **d**, Identified metabolites in faecal samples collected from non-antibiotic-treated versus antibiotic-treated participants as measured by LC–MS. Area under the curve (AUC) values are presented relative to each metabolite's

normalized average (normalized to 1) within the dataset as measured by LC–MS. See Supplementary Table 4 for original data. **e**, Identified metabolites in mouse faeces pre-antibiotic and post-antibiotic treatment. AUC values are presented relative to each metabolite's normalized average (normalized to 1) within the dataset. Grey boxes highlight reductase substrate and product pairs. See Supplementary Table 5 for original data. For **a**, data are mean \pm s.d. ($n = 3$ independent biological replicates) with two-way ANOVA, multiple test versus media alone. For **d**, data are mean \pm s.e.m. ($n = 21$ antibiotic treated, 20 untreated) with multiple unpaired *t*-tests. For **e**, $n = 6$ pre-antibiotic treated and $n = 6$ post-antibiotic treated, with multiple unpaired *t*-tests. * $P < 0.05$; ** $P < 0.01$; *** $P < 0.001$.

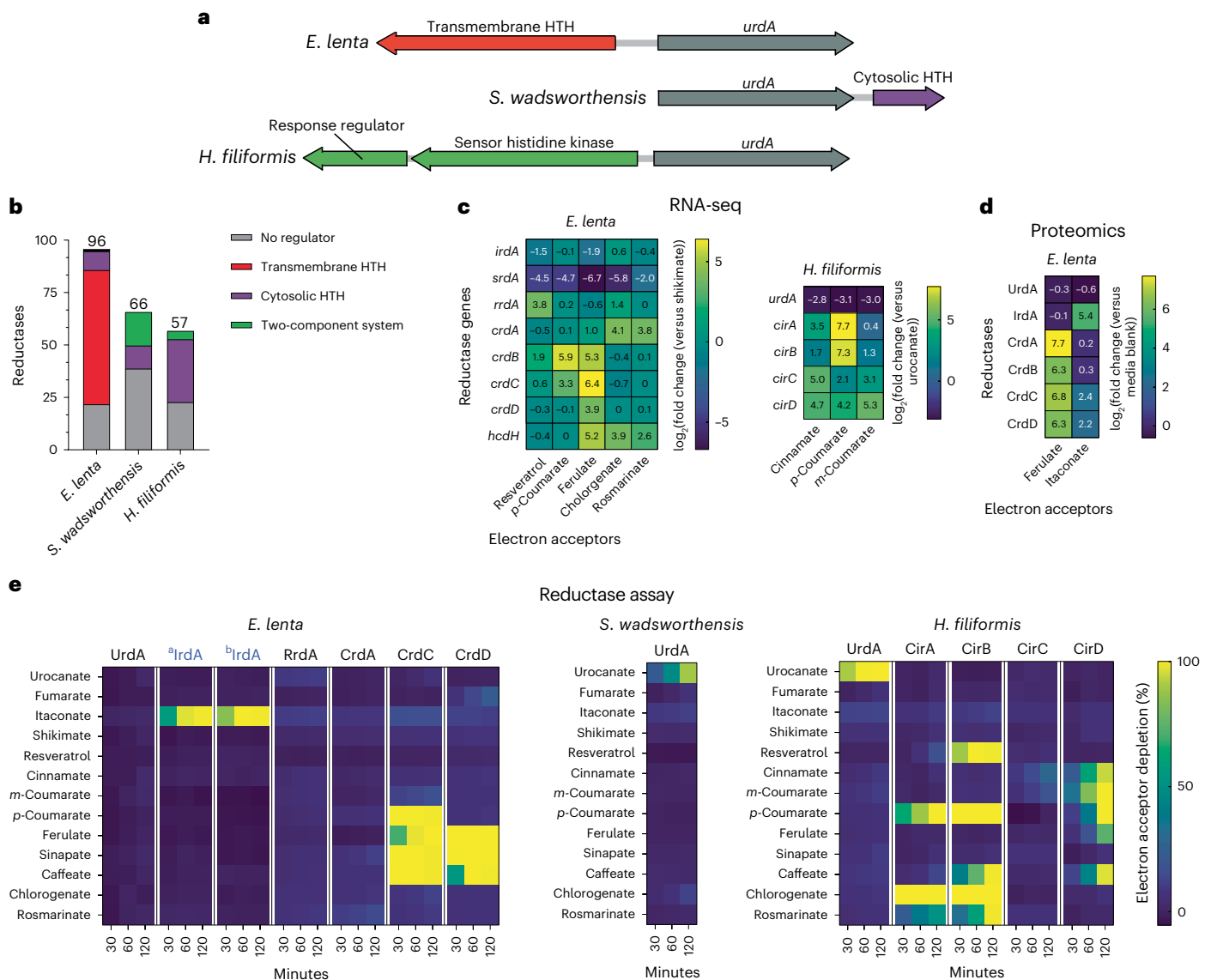


Fig. 4 | Flavin reductases are induced by their electron acceptors and exhibit relatively narrow substrate specificities. a, Genomic context of *urdA* urocanate reductases in *E. lenta* DSM2243, *S. wadsworthensis* DFI.4.78 and *H. filiformis* DFI.9.20 genomes. Genes encoding predicted transcriptional regulators are noted. **b**, Genomic context of flavin and molybdopterin reductases with respect to adjacent regulatory elements: no clear element present (grey), two-component system (green), cytosolic regulator (purple) or transmembrane regulator (red). Cytosolic and transmembrane refer to the cellular localization of

the putative signal-receiving domain in predicted transcriptional regulators that contain a DNA-binding HTH domain. **c**, RNA-seq results from *E. lenta* DSM2243 and *H. filiformis* DFI.9.20 cells cultivated in media supplemented with indicated electron acceptors. **d**, Proteomics results from *E. lenta* DSM2243 cells cultivated in media supplemented with indicated electron acceptors. **e**, Activity of recombinant reductases in the presence of indicated electron acceptors. IrdA (**a**) and IrdA (**b**) are IrdA orthologues from *A. muris* and *B. wangjianweii*, respectively. For **e**, representative data are shown.

Supplementary Table 6)³⁶. As bacterial transcriptional regulators often establish autoregulatory circuits that concordantly regulate neighbouring genes on the genome, we reasoned that it might be possible to leverage transcriptional responses to respiratory electron acceptors to gain insight into reductase substrate specificity.

After confirming the predicted *E. lenta* urocanate reductase was one of the most strongly induced genes in the presence of urocanate, we performed RNA sequencing (RNA-seq) on *E. lenta* and *H. filiformis* in nine conditions containing a respiratory electron acceptor used by an unknown reductase (Fig. 4c and Supplementary Tables 7 and 8). We further performed proteomic analyses of *E. lenta* grown in the presence of ferulate and itaconate to identify reductase induction at the protein level (Fig. 4d and Supplementary Table 9). From these experiments, we identified at least one flavin reductase as among the most strongly

induced genes in the presence of each electron acceptor. To facilitate downstream analyses, we assigned reductase gene names based on the condition they were induced (crdA for the *E. lenta* cinnamate-induced reductase A, cirB for the *H. filiformis* cinnamate-induced reductase B and so on; Supplementary Table 10).

Next, we compared reductase expression across conditions and observed a complex pattern of regulation. While itaconate, shikimate and resveratrol each specifically induced a single flavin reductase, distinct cinnamates differentially induced multiple flavin reductases (Fig. 4c,d). For both *E. lenta* and *H. filiformis*, structurally related cinnamates resulted in elevated but variable expression of four distinct flavin reductases (Fig. 4c). Furthermore, in *E. lenta*, ferulate and chlorogenicate, but not *p*-coumarate, induced the previously characterized hydrocaffeate dehydroxylase *hcdH* (Fig. 4c)⁹. These findings thus reveal

specific but sometimes complex regulatory responses of reductases to related respiratory electron acceptors.

Reductase induction predicts substrate specificity

To assess whether gene expression patterns could predict enzyme substrate specificity, we recombinantly expressed 13 flavin reductases identified in our transcriptomics and proteomics studies (Extended Data Fig. 9). Due to poor yields of the *E. lenta* itaconate-induced reductase, IrdA, we additionally expressed two close IrdA orthologues from *Adlercreutzia muris* and *Berryella wangjianwei* (^aIrdA and ^bIrdA, respectively). Purified reductases were assayed on a panel of identified electron acceptors. Ten purified reductases reduced at least one electron acceptor, with substrate specificity strongly tracking with the observed induction patterns (Fig. 4e). To further validate assigned substrate specificities, we tested whether *irdA* predicted strain-level variability in *E. lenta* itaconate utilization. Indeed, we found that the presence of *irdA* predicted itaconate reduction across five different *E. lenta* strains (Extended Data Fig. 10).

Substrate-profiling experiments revealed particularly marked distinctions in cinnamate reductase substrate specificity. While the ability of *E. lenta* and *H. filiformis* to use diverse cinnamates could plausibly reflect the activity of a single promiscuous reductase, we found that both microorganisms encode multiple reductases with distinct specificities for different subsets of cinnamates (Fig. 4e). Among *H. filiformis* reductases, CirA used *p*-coumarate, chlorogenate and rosmarininate. CirC weakly used cinnamate, while CirD used cinnamate, *m*-coumarate, *p*-coumarate, ferulate and caffeate. Intriguingly, while the cinnamate reductase CirB used *p*-coumarate, caffeate, chlorogenate and rosmarininate, it also used the alkene resveratrol. Among *E. lenta* reductases, CrdC and CrdD both used sinapate, ferulate and caffeate, with CrdC uniquely using *p*-coumarate. These results show that *E. lenta* and *H. filiformis* express multiple cinnamate reductases with variable substrate specificities, some of which discriminate between substrates with relatively subtle structural differences.

Reductases exhibit evolutionary complexity

We next explored the relationship between reductase evolution and substrate specificity. We reasoned that new reductase activities could be acquired either by (1) horizontal gene transfer or (2) gene duplication followed by functional divergence, and that these two scenarios would lead to distinct relationships between reductase sequence and substrate specificity. To investigate this, we constructed a phylogenetic tree using flavin reductases from *E. lenta*, *S. wadsworthensis* and *H. filiformis* genomes (Fig. 5).

Several branches in the resulting tree include reductases from multiple species. For example, urocanate reductases from the three species are monophyletic and thus presumably share a more recent common evolutionary history (Fig. 5). However, a majority of branches on the tree are highly sub-branched and exclusively contain reductases from a single genus. These patterns suggest that both horizontal gene transfer and gene duplication may have played substantial roles in reductase evolution within bacterial lineages.

The distribution of reductases with different activities in the tree suggests a convoluted evolutionary history, with cinnamate reductases providing a striking example of the complex relationship between amino acid sequence and substrate specificity. We observed that, despite catalyzing highly similar reactions, the eight *E. lenta* and *H. filiformis* reductases induced in the presence of different cinnamate substrates separated into four phylogenetically distinct reductase clades (Fig. 5, clades 1–4). Identified cinnamate reductases typically share >30% amino acid sequence identity with other reductases within their clade—including reductases with distinct substrate specificities. For example, *H. filiformis* cinnamate reductase CirD and urocanate reductase UrdA are both from ‘reductase clade 1’ and share 32% sequence identity. By contrast, the cinnamate reductases from

different reductase clades share <26% sequence identity, despite using similar substrates (Fig. 5). The observations suggest that flavin reductases with similar cinnamate substrate specificities independently evolved at least four times.

Dissimilar reductase active sites catalyze related reactions

To clarify how different evolutionary trajectories may have independently generated reductases with similar cinnamate substrate specificities, we turned to previous mechanistic studies of enzymes from the flavin reductase superfamily. Fumarate and urocanate reductases were previously shown to contain two conserved active-site arginines—one that forms a critical salt bridge with the substrate carboxyl group and a second proposed to facilitate catalytic proton transfer to reduce the substrate enoate group^{37–39}. As a similar substrate enoate group is reduced by cinnamate reductases, we compared the substrate-bound urocanate reductase crystal structure with AlphaFold structural models of cinnamate reductases from the four reductase clades (Fig. 5). We found that active-site arginines were conserved in reductase clade 1, including in the UrdA urocanate reductases and the CirD cinnamate reductase (Fig. 5, alignment positions 4 and 6). By contrast, arginines were not conserved at the same positions in reductase clades 2–4. Instead, tyrosine was conserved at alignment position 6 and other active-site amino acids exhibited variable, clade-specific patterns of conservation (Fig. 5).

To test whether the distinct patterns of active-site conservation in the four reductase clades might reflect mechanistic distinctions, we generated point mutants that targeted conserved amino acids in representative cinnamate reductases (CirA, CirC, CirD and CrdD) from reductase clades 1–4. In each case, we found that conserved clade-specific active-site amino acids were essential for activity (Fig. 5). These results thus show that distinct active-site architectures functionally distinguish the cinnamate reductase clades and suggest that parallel evolutionary processes produced flavin reductases with similar substrate specificities but substantial functional distinctions (see Supplementary Discussion for additional analysis).

Discussion

Here we identify taxonomically distinct members of the gut microbiome that possess high numbers of respiratory-like reductases per genome. We find that these bacteria possess respiratory metabolisms and identify organic respiratory electron acceptors that exhibit strain-dependent patterns of usage. While much remains to be explored about the role of these activities, our results suggest that a distinct type of respiration, defined by the versatile use of diverse organic respiratory electron acceptors, may play important roles within the gut.

Notably, the bacteria identified in our studies possess reductase arsenals (often >50 reductases per genome) that stand apart from previously characterized (non-host associated) bacterial respiratory specialists. For example, the marine and fresh-water-inhabiting bacterium *Shewanella oneidensis* is widely cited as a model organism with exceptionally broad respiratory capabilities, but possesses ‘only’ 22 molybdopterin and flavin reductases (Supplementary Table 2)^{40–42}.

Perhaps related to this observation, most characterized respiratory electron acceptors used by non-host-associated respiratory specialists like *S. oneidensis* are small inorganic compounds. By contrast, the respiratory electron acceptors identified in our studies are primarily organic metabolites. Host feeding produces a consistent influx of organic compounds that likely distinguishes the gut from many other microbial ecosystems. It thus stands to reason that the dramatic reductase expansion in gut bacteria may reflect the enzymatic diversity required to match the high concentration of chemically complex metabolite electron acceptors present in the gut. These observations suggest that ecosystem-dependent ecological differences may explain the emergence of distinct respiratory strategies defined by (1) a large reductase arsenal and respiration of diverse metabolite electron

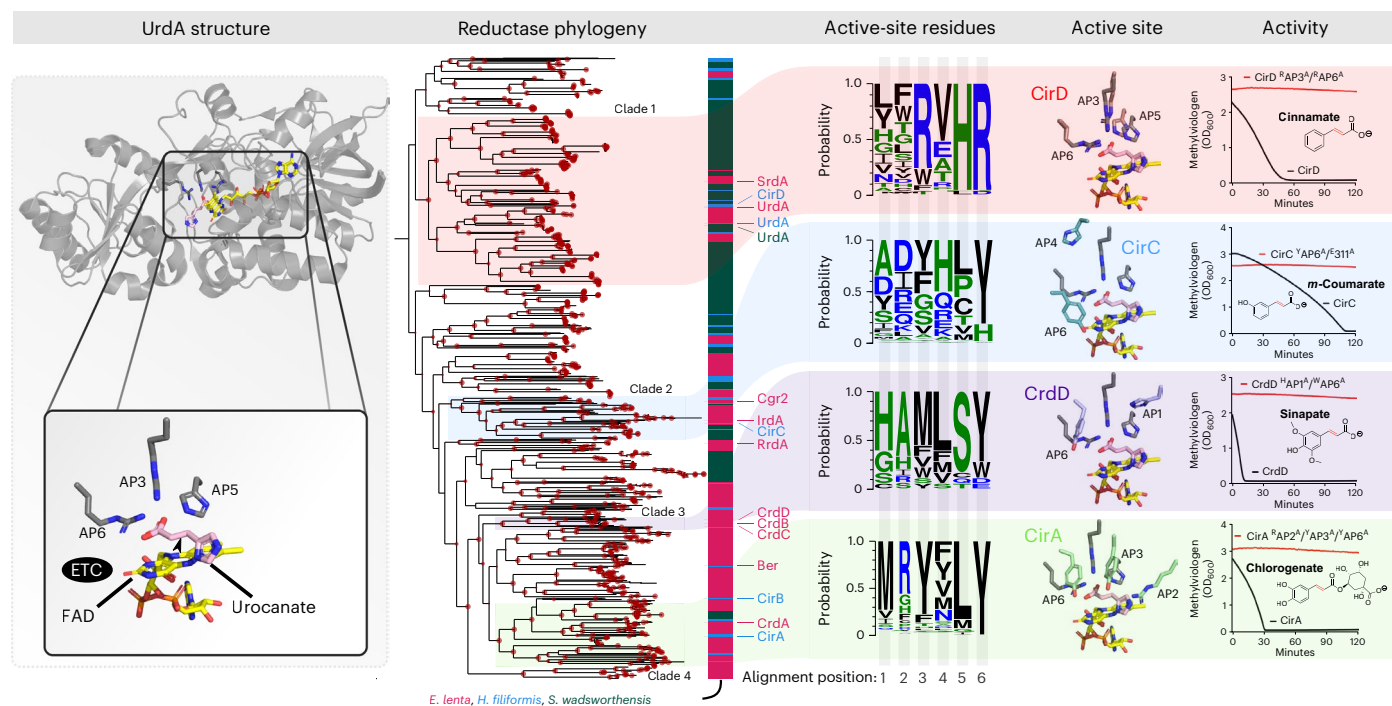


Fig. 5 | Independent evolutionary trajectories and distinct active sites distinguish flavin reductases with related electron acceptors. UrDA structure—previously published crystal structure of the *S. oneidensis* UrDA in complex with urocanate and flavin adenine dinucleotide (FAD) (PDB code 6T87). Reductase phylogeny—phylogenetic tree of flavin reductases from *E. lenta*, *S. wadsworthensis* and *H. filiformis* genomes. Bootstrap support values are indicated by the size of the red dots at nodes of the tree and range from 70 to 100. Active-site residues—representation of the sequence identity of active-site amino acids in reductase clades 1–4 scaled to frequency within the multiple

sequence alignment. Positions within the multiple sequence alignment have been renumbered to active-site alignment position (AP). Active site—AlphaFold models of CirD, CirC, CrdD and CirA cinnamate reductases superimposed on the UrDA crystal structure. Activity—reductase activity of CirD, CirC, CrdD and CirA and active-site point mutants. Active-site mutations and alignment positions they correspond to: CrdD H313A (AP1) and W510A (AP6); CirA R417A (AP2), Y469A (AP3) and Y634A (AP6); CirC E311A and Y511A (AP6); CirD R542A (AP3) and R716A (AP6). The y-axis shows the amount of reduced methyl viologen in the presence of the indicated electron acceptor.

acceptors versus (2) a smaller reductase arsenal and respiration of fewer inorganic compounds.

A particularly important aspect of the respiratory metabolisms identified in our studies concerns their implication for the gut metabolome. Microbiome-derived imidazole propionate, the product of urocanate reduction, impairs insulin signalling through mTORC1 and is elevated in the serum of patients with type 2 diabetes⁴³. Microbiome-derived hydro-*p*-coumarate (also called 4-hydroxyphenylpropionate or desaminotyrosine) protects against influenza through type I interferon activation^{44,45}. Resveratrol impacts multiple enzymes and transcription factors and influences several metabolic and immune pathways³³.

Further pointing to the importance of respiration in the metabolism of bioactive metabolites, several *E. lenta* reductases with electron acceptors relevant for mammalian physiology have been previously described. Cgr2 is a flavin reductase that reduces the cardiac medication digoxin and an unidentified molecule that drives intestinal inflammation through Th17 activation^{36,46–48}. The flavin reductase Ber catalyzes a carbon–oxygen bond cleavage as part of a pathway that generates enterodiol and enterolactone, compounds that function similarly to the endogenous hormone oestrogen⁴⁹. Finally, Dadh is a molybdopterin reductase that dehydroxylates the neurotransmitter dopamine and inactivates the Parkinson's disease medication L-DOPA^{9,50}.

Itaconate is perhaps the most intriguing electron acceptor identified in our studies. In macrophages, itaconate is produced by the interferon-inducible gene Irg1 in response to bacterial and viral infection. In this context, itaconate acts as an immunometabolite that orchestrates direct and indirect mechanisms of pathogen defence^{33–35}. Several intracellular bacterial pathogens counteract

mammalian itaconate by degrading it to pyruvate and acetyl-CoA^{51,52}. The reduction of itaconate to 2-methylsuccinate by itaconate reductase represents a second type of bacterial transformation of itaconate. 2-Methylsuccinate has received little attention from previous research, although a recent preprint reported that levels of 2-methylsuccinate and itaconate increase in the bile following infection with multiple intestinal bacterial pathogens⁵³. While, to our knowledge, neither itaconate nor 2-methylsuccinate has been studied within the gut, it is striking that both compounds are dramatically reduced in faecal samples from an antibiotic-treated population (Fig. 3d).

In conclusion, our studies establish a respiratory strategy defined by the use of a large reductase arsenal to access diverse metabolite electron acceptors. We show that reactions catalyzed by respiratory reductases effect various bioactive metabolites. Considering that the vast majority of reductases encoded by gut bacteria remain functionally uncharacterized, identified metabolisms may only scratch the surface of interactions between respiratory reductases and the gut metabolome. Continued study of respiratory electron acceptor usage may thus provide an important avenue for informing our understanding of the functional capacity and metabolic output of the gut microbiome.

Methods

Detection of molybdopterin and flavin reductases

Genomes and metagenome-assembled genomes of common prokaryotes in the human gut microbiome were downloaded from version 2.0 of the Unified Human Gastrointestinal Genome in MGnify database on July 2022³¹. Only species-representative genomes identified in more than five distinct samples (1,533 in total) were included in subsequent analyses. Gene prediction was done with Prodigal (version 2.6.3)⁵⁴ in

single mode. Molybdopterin and flavin reductases were identified by searching Pfam database HMMs (PF00384 and PF00890, respectively) with the tool Hmmssearch (version 3.3; e-value cut-off 0.001)^{55,56}. SignalP (version 5.0) was run to predict the putative cellular localization of the proteins using the parameter -org gram⁵⁷.

To extend the genomic reductase content analyses to the identified taxonomic families, selected representative genomes for Burkholderiaceae, Eggerthellaceae and Erysipelotrichaceae (Extended Data Fig. 1a–c and Supplementary Table 3) were downloaded from the Genome Taxonomy Database in October 2022 (release 202 of 27 April 2021). The same protocol as described above was performed to detect the flavin and molybdopterin reductases.

Concatenated ribosomal protein phylogeny

Maximum-likelihood trees were calculated based on the concatenation of 14 ribosomal proteins (L2, L3, L4, L5, L6, L14, L15, L18, L22, L24, S3, S8, S17 and S19) for the Unified Human Gastrointestinal Genome tree and 16 ribosomal proteins (the 14 ribosomal proteins mentioned plus L16 and S10) for the Burkholderiaceae, Eggerthellaceae and Erysipelotrichaceae family trees. Homologous protein sequences were aligned using MAFFT (version 7.467; –auto option), and alignments refined to remove gapped regions using Trimal (version 1.4.1; –gap-ppout option)^{58,59}. The protein alignments were concatenated and manually inspected. Phylogenetic trees were inferred using IQ-TREE (version 1.6.12) with 1,000 ultrafast bootstrap replicates (–bnni-m TEST-st AA-bb1000-nt AUTO), using ModelFinder to select the best model of evolution, and with 1,000 ultrafast bootstrap^{60–62}.

Reductase pangenomics

Pangenomes for *E. lenta*, *S. wadsworthensis* and *H. filiformis* were calculated using anvi'o 7.1 (with parameters anvi-pan-genome –mcl-inflation 10)⁶³. Briefly, the program (1) performed an all-versus-all National Center for Biotechnology Information (NCBI) BLAST to create a sequence similarity network, (2) used the Markov Cluster algorithm to resolve gene clusters and (3) was visualized with ‘anvi-display-pan’⁶⁴. Subsequently, the species pangenomes were subsetted for gene clusters annotated with the Pfam PF00890 using ‘anvi-split’.

General bacterial culture conditions

All bacterial strains used in this study are listed in Supplementary Table 11. Anaerobic growth was performed in a Coy vinyl anaerobic chamber under an atmosphere of 2–5% H₂, 2–5% CO₂ and balance nitrogen. Strains used in this study were initially grown on brain–heart infusion (BHI) media (BD BACTO, 237500) plates for 48–72 h at 37 °C to yield visible colonies. Overnight cultures were grown for 24 h at 37 °C using liquid BHI for *E. lenta* and *S. wadsworthensis*, or liquid BHI-NoDex (Alpha Bioscience Brain Heart Infusion W/O Dextrose, B02-114) plus 0.01% Tween 80 for *H. filiformis*.

ATP assay

Bacterial cultures were grown and conditioned overnight in 10 mM sodium formate and 10 mM electron acceptor to induce reductase expression. Cells were washed and resuspended in phosphate assay buffer (40 mM potassium phosphate, 10 mM magnesium sulfate, pH 7.0) then allowed to incubate at room temperature for 45 min to achieve a resting cell suspension. To initiate the reaction, cells were mixed 1:1 with buffer containing 2 mM sodium formate or buffer containing 2 mM sodium formate additionally supplemented with 2 mM electron acceptor in a 96-well plate. At specified time points, 10 µl of mixture was taken out and placed into a separate 96-well plate with 90 µl DMSO to quench the reaction and liberate cellular ATP. The ATP concentration was measured by using an ATP determination kit (Invitrogen A22066). Sample luminescence was read using black well plates (Corning 96-well black 3915) in a BioTek Cytation 5 plate reader and compared to a standard curve of known ATP concentrations.

Respiratory electron acceptor screen

A collection of potential respiratory electron acceptors were selected for testing based on (1) their likely presence in the gut, (2) commercial availability and (3) previous reports of their reduction by species in the Eggerthellaceae family (in the case of some phenylpropanoid derivatives)^{9,49,65}. Selected potential electron acceptors were directly dissolved into media at 10 mM in either 50% BHI medium containing 10 mM sodium formate (*E. lenta* and *S. wadsworthensis*) or 100% BHI-NoDex with 0.01% Tween 80 (*H. filiformis*) and filter sterilized. Molecules were not dissolved in solvents first to avoid potential issues of their additional usage by bacteria. The medium was arrayed into deep-well (1 ml) 96-well plates (USA Scientific PlateOne 1896-1110) for growth. Strains were inoculated with normalized 1:1,000 inoculations from overnight cultures, and plates were sealed with adhesive seals to minimize evaporation. Time points were taken at 24, 48, 72 and 96 h by mixing with a multichannel pipette and moving 200 µl into a separate 96-well plate (Greiner Bio-One 96-well microplates 658162) and reading absorbance at OD₆₀₀ (optical density at 600 nm) in a BioTek Cytation 5 plate reader normalized to media blanks.

Metabolite extraction from liquid culture

Samples were incubated at –80 °C between 1 h and 12 h. Four volumes of methanol containing internal standards (d⁷,¹⁵N-proline (Cambridge Isotope Laboratories, DNLM-7562) and U-¹³C-palmitic acid (Cambridge Isotope Laboratories, CLM-409)) were added to each culture supernatant (one volume) in a microcentrifuge tube. The tubes were then centrifuged at –10 °C and 20,000 × g for 15 min followed by the transfer of 100 µl of supernatant to pre-labelled mass spectrometer autosampler vials (MicroLiter, 09-1200).

Metabolite extraction from faecal material

Metabolites were extracted from faecal samples by adding 80% methanol (containing ¹³C₉-phenylalanine (CLM-2250), d₆-succinate (DLM-831) and ¹³C₁₁-tryptophan (CLM-4290) internal standards (Cambridge Isotope Laboratories)) to 100 mg ml⁻¹ and stored at –80 °C for at least 1 h in beadruptor tubes (Fisherbrand, 15-340-154). Samples were then homogenized at 4 °C on a Bead Mill 24 Homogenizer (Fisherbrand, 15-340-163) set at 1.6 m s⁻¹ with six 30 s cycles, 5 s off per cycle. Samples were then centrifuged at –10 °C, 20,000 × g for 15 min to generate supernatants for subsequent metabolomic analysis.

Derivatization methods for GC–MS analyses

Culture supernatants were dried completely under a nitrogen stream at 30 °C (Biotage SPE Dry 96 Dual, 3579M). To dried samples, 50 µl of freshly prepared 20 mg ml⁻¹ methoxamine (Sigma, 226904) in pyridine (Sigma, 270970) was added and incubated in a ThermoMixer (Eppendorf) for 90 min at 30 °C and 1,400 rpm. After the samples were cooled to room temperature, 80 µl of derivatizing reagent (*N,O*-bis(trimethylsilyl)trifluoroacetamide, 1% trimethylchlorosilane; Sigma, B-023) and 70 µl of ethyl acetate (Sigma, 439169) were added and mixed in a ThermoMixer at 70 °C for 1 h at 1,400 rpm. The samples were cooled to room temperature and diluted with 400 µl of ethyl acetate for analysis.

GC–MS chromatography and instrument parameters

Culture supernatants were analysed using GC–MS (Agilent 7890A GC system, Agilent 5975C MS detector) with an electron impact ionization source, a HP-5MSUI column (30 m × 0.25 mm, 0.25 µm; Agilent Technologies 19091S-433UI) and 1 µl injection. Oven ramp parameters were as follows: 1 min hold at 60 °C and 16 °C min⁻¹ up to 300 °C with a 7 min hold at 300 °C, for a total run time of 23 min. The inlet temperature was 280 °C, the transfer line was 300 °C and the source temperature was 230 °C. Ionization was achieved using a 70 eV electron beam. Ions were measured over a 50–600 m/z range.

GC–MS data analyses

Culture supernatant data analyses were performed using MassHunter Quantitative Analysis software (version B.10, Agilent Technologies). Metabolite identifications were confirmed by matching to authentic standard spectra and retention time and spectra in the NIST Tandem Mass Spectral Library version 2.3 (see Supplementary Tables 12 and 13 for background and validation methods of each metabolite). Thus, all metabolites reported from mouse faecal pellet samples and human stool samples are identified at confidence level 1⁶⁶. Normalized peak areas were calculated by dividing raw peak areas of targeted analytes by averaged raw peak areas of internal standards d7-proline and U-¹³C-palmitate.

LC–MS parameters for culture supernatant analyses

Catechin, epicatechin, chlorogenate, rosmarinic acid and shikimate reduction products were not readily available as standards; therefore, LC–MS/MS fragmentation was used to identify putative products of these reduction reactions in microbial cultures. All LC–MS analyses were performed using a Thermo Scientific Vanquish Flex UHPLC coupled to an IQ-X mass spectrometer (Thermo Fisher Scientific). To detect these compounds and their putative reduced products in *E. lenta* and *S. wadsworthensis* cultures, the chromatographic method used was an isocratic 100% mobile phase A (5% acetonitrile, 0.1% formic acid in water) for 0.2 min, followed by a gradient of 0 to 97% mobile phase B (99.9% acetonitrile, 0.1% formic acid) for 4.5 min with a wash of 100% mobile phase B for 1 min. Catechin, epicatechin, chlorogenate, rosmarinic acid and shikimate and their putative reduced products were detected by mass spectrometry using negative ionization. Flow from the UHPLC was ionized with the HESI source set to 2,400 V, ion transfer tube temperature set to 200 °C, vaporizer temperature set to 400 °C, and sheath, auxiliary and sweep gases set to arbitrary values of 40, 5 and 1, respectively. Data for MS¹ were acquired using a maximum injection time of 50 ms, a normalized automatic gain control (AGC) target of 25%, a 100–1,300 m/z quadrupole scan range and a resolution of 60,000. All tandem MS² mass spectral data were acquired using a 1.5 m/z quadrupole isolation window, a maximum injection time of 22 ms, a normalized AGC target of 20% and a resolution of 15,000. Each of the metabolite ions of interest was added to an inclusion list for MS² fragmentation by a normalized higher-energy collisional dissociation energy of 30%. Standards for catechin and epicatechin reduction products, hydrochlorogenate, hydro-rosmarinic acid and hydroshikimate (3,4,5-trihydroxycyclohexanecarboxylic acid) were not readily available; therefore, they are reported at confidence level 3 (ref. 66). To support the identification of the putative catechin and epicatechin reduction products, a comparison of the derivative MS² fragmentation spectra with a representative catechin and epicatechin MS² fragmentation spectrum has been included (Supplementary Figs. 1 and 2). To support the assignment of the hydrochlorogenate and hydro-rosmarinic acid structures, analysis of the MS² fragmentation spectrum and a comparison with the hydrochlorogenate and hydro-rosmarinic acid MS² fragmentation spectra, respectively, have been included with putative fragment ion structures (Supplementary Figs. 3 and 4). To support the assignment of the hydroshikimate structure, analysis of the MS² fragmentation spectrum and a comparison to the shikimate MS² fragmentation spectrum have been included with putative fragment ion structures (Supplementary Fig. 5).

LC–MS parameters for faecal material analyses

All metabolites from mouse faecal pellet and human stool were measured by LC–MS analyses. Reversed-phase chromatography was performed at a 300 µl min⁻¹ flow rate on a Waters CORTECS T3 C18 RP-UHPLC column (100 × 2.1 mm inner diameter, 1.6 µm particle size, 120 Å pore size (1 Å = 0.1 nm)). Mobile phase A was 5% acetonitrile in water with 0.1% formic acid, and mobile phase B was acetonitrile with 0.1% formic acid. For all mouse faecal pellet and human stool analyses,

the chromatographic method used was an isocratic 100% mobile phase A for 0.2 min, followed by a gradient of 0 to 40% mobile phase B for 2.8 min, then a gradient from 40% to 100% mobile phase B over 1.5 min, with a final wash of 100% mobile phase B for 1.5 min. To acquire negative ionization mass spectra, flow from the UHPLC was ionized with the HESI source set to 3,500 V, ion transfer tube temperature set to 190 °C, vaporizer temperature set to 120 °C, and sheath, auxiliary and sweep gases set to arbitrary values of 50, 10 and 1, respectively. For positive ionization mass spectra, flow from the UHPLC was ionized with the HESI source set to 3,500 V, ion transfer tube temperature set to 300 °C, vaporizer temperature set to 350 °C, and sheath, auxiliary and sweep gases set to arbitrary values of 50, 10 and 1, respectively. Data for both positive- and negative-mode MS and MS² were acquired using the EASY-IC internal calibration to fluoranthene, automatic maximum injection time and standard AGC target. Furthermore, data for all MS¹ were acquired using a 100–365 m/z quadrupole scan range and a resolution of 120,000. All tandem MS² mass spectral data were acquired using a 0.7 m/z quadrupole isolation window and a resolution of 15,000. Each of the metabolite ions of interest was added to an inclusion list for MS² fragmentation by stepped higher-energy collisional dissociation absolute energies of 20, 40, 60 and 80 eV.

LC–MS data analysis

Mouse faecal pellet and human stool sample data analysis was performed using FreeStyle software (version 1.8 SP2, Thermo Scientific). Metabolite identification was established by matching accurate mass, retention time and MS² fragmentation pattern from candidate ions in experimental samples to data from authentic standards of each metabolite of interest. Thus, all metabolites reported from mouse faecal pellet samples and human stool samples are identified at confidence level 1⁶⁶. Normalized peak areas were calculated by dividing raw peak areas of targeted analytes by averaged raw peak areas of internal standards (¹³C₉-phenylalanine and ¹³C₁₁-tryptophan for metabolites measured by positive ionization; d₆-succinate and ¹³C₁₁-tryptophan for metabolites measured by negative ionization).

GC–MS and LC–MS quality control

Biological control plasma samples were processed and analysed alongside culture supernatant samples to evaluate metabolite extraction efficiency and instrument performance. The samples were extracted with methanol containing known internal standard concentrations. The recovery, retention time and coefficient of variation were calculated for the internal standards. Method blanks containing no metabolites were included throughout the run.

Collection of mouse faecal samples

All mouse experiments were performed in accordance with and approved by the Institutional Animal Care and Use Committee of the University of Chicago under protocol 72599. Female specific-pathogen-free C57BL/6 mice, aged 6 weeks to 9 weeks, from Jackson Laboratories were used for all experiments. Mice were kept within a facility that maintained a 12 hour light and 12 hour dark cycle and controlled humidity (30–70%) and temperature (68–79 °F). Mice were housed in sterile, autoclaved cages with irradiated feed (LabDiet 5K67) and acidified, autoclaved water upon arriving at the on-site mouse facility. Mouse handling and cage changes were performed by investigators wearing sterile gowns, masks and gloves in a sterile biosafety hood. Mice were cohoused with their original shipment group until after antibiotic treatment. Fresh faecal pellets were collected directly from mice.

Following collection of ‘pre-antibiotic’-treatment faecal pellets, mice were administered metronidazole, neomycin and vancomycin each at 0.25 g l⁻¹ in drinking water for 3 days. The drinking water was then changed to acidified, autoclaved water, and the mice were transferred to clean cages. Mice were injected intraperitoneally with

clindamycin 0.4 mg total, 2 days after the end of the metronidazole, neomycin and vancomycin regimen, and received a cage change each day following to prevent additional antibiotic consumption through coprophagy. 'Post-antibiotic'-treatment faecal pellets were collected 2 days after the clindamycin injection.

Collection of human faecal samples

Faecal samples from healthy, non-antibiotic-treated participants (13 females and 6 males, age range = 18–60 years, average age = 35 years) were collected through a prospective faecal collection protocol (University of Chicago Protocol IRB20-1384) approved by the institutional review boards (IRB) at the University of Chicago. All donors provided written and informed consent for IRB-approved biospecimen collection and analysis. The study was conducted in accordance with the Declaration of Helsinki.

Faecal samples (9 females and 13 males, age range = 32–77 years, average age = 54 years) from patients treated with broad-spectrum antibiotics were selected from samples collected as part of a prospective cohort study of hospitalized adult hepatology patients at a single institution⁶⁷. Inclusion criteria for the study included age \geq 18 years, ability to provide informed consent (either themselves or by proxy if decisionally incapacitated) and being treated on the hepatology consult service. Participants who were younger than 18 years, were unable to provide consent, had previous solid organ transplant or had a previous colectomy were excluded. Patients were enrolled as soon as possible upon hospital admission, most within 48 h. All samples were obtained under a protocol that was approved by the University of Chicago IRB (IRB21-0327), and written informed consent was obtained from all participants or their surrogate decision-makers.

Upon collection, faecal samples were refrigerated at +4 °C for less than 24 h before aliquoting and storing at –80 °C until processing for shotgun metagenomic and metabolomic analysis (details below). Demographic and clinical data, including medication administration, were collected through a review of the medical record and through the University of Chicago Center for Research Informatics.

A total of 22 samples from the antibiotic-treated patients included in this study were chosen based on antibiotic administration and metagenomic findings that would be expected after broad-spectrum antibiotic exposure. The most common antibiotic exposure was a combination of intravenous (IV) vancomycin, IV cefepime and IV metronidazole; however, one patient was also exposed to meropenem, two patients to piperacillin–tazobactam and one patient to ciprofloxacin and ceftriaxone. The metagenomic changes included 8 samples with >90% relative abundance of Proteobacteria and 14 samples with >90% relative abundance of *Enterococcus*, which indicates that broad-spectrum antibiotic exposure had marked effects on the gut microbiome composition in these samples.

Faecal DNA extraction

DNA was extracted using the QIAamp PowerFecal Pro DNA kit (Qiagen). Before extraction, samples were subjected to mechanical disruption using a bead beating method. Briefly, samples were suspended in a bead tube (Qiagen) along with lysis buffer and loaded on a bead mill homogenizer (Fisherbrand). Samples were then centrifuged, and the supernatant was resuspended in a reagent that effectively removed inhibitors. DNA was then purified routinely using a spin column filter membrane and quantified using Qubit.

Metagenomic analyses of human faecal samples

Human faecal samples underwent shotgun DNA sequencing. After undergoing mechanical disruptions with a bead beater (BioSpec Product), samples were further purified with QIAamp mini spin columns (Qiagen). Purified DNA was quantified with a Qubit 2.0 fluorometer and sequenced on the Illumina HiSeq platform, producing around 7 to 8 million paired-end reads per sample with read length of 150 bp.

Adaptors were trimmed off from the raw reads, and their quality was assessed and controlled using Trimmomatic (v.0.39); then, the human genome was removed by kneaddata (v0.7.10, <https://github.com/biobakery/kneaddata>)⁶⁸. Taxonomy was profiled using metaphlan4 (ref. 69). The alpha diversity (a reflection of the number of unique bacterial taxa and their relative abundances) of faecal samples was estimated using the inverse Simpson index. Raw sequencing data generated were deposited to the NCBI Sequence Read Archive under accession number PRJNA912122.

16S amplicon sequencing analyses of mouse faecal samples

The V4–V5 region within the 16S ribosomal RNA (rRNA) gene was amplified using universal bacterial primers—563F (5'-nnnnnnnn-NNNNNNNNNNNN-AYTGGGYDTAAA-GNG-3') and 926R (5'-nnnnnnnn-NNNNNNNNNNNN-CCGTCATTYHT-TTRAGT-3'), where 'N' represents the barcodes and 'n' is an additional nucleotide added to offset primer sequencing. Amplicons were then purified using magnetic beads, then quantified and pooled at equimolar concentrations. Illumina sequencing-compatible combinatorial dual index adapters were ligated onto pooled amplicons using the QIAseq one-step amplicon library kit (Qiagen). Library quality control was performed using Qubit and TapeStation and sequenced on an Illumina MiSeq platform to generate 2 × 250 bp reads, generating 5,000–10,000 reads per sample. Raw V4–V5 16S rRNA gene sequence data are demultiplexed and processed through the dada2 pipeline into amplicon sequence variants (ASVs) with minor modifications in R (v4.0.3). Specifically, reads were first trimmed at 210 bp for forward reads and 150 for reverse reads to remove low-quality nucleotides. Chimeras were detected and removed using the default consensus method in the dada2 pipeline. Then, ASVs with length between 300 bp and 360 bp were kept and deemed as high-quality ASVs. The taxonomy of the resultant ASVs was assigned to the genus level using the RDP Classifier (v2.13) with a minimum bootstrap confidence score of 80. Species-level classification can be provided using blastn (v2.13.0) and refseq_rna database (updated June 10 2022).

Transcriptomics analyses

E. lenta and *H. filiformis* were grown in 50 ml of medium supplemented with 10 mM formate and 10 mM of the tested electron acceptor. A BHI baseline medium was used for *E. lenta* cultures. A no-dextrose BHI medium supplemented with 0.01% Tween 80 was used for *H. filiformis* cultures. Overnight cultures were diluted 1:100 into flasks and allowed to grow, shaking for 24 h. Whole cultures were pelleted and used for RNA extraction. Total RNA from biological replicates was extracted using the Maxwell RSC instrument (Promega). RNA was quantified using Qubit, a fluorometric method, and integrity was measured through a TapeStation (Agilent Technologies). Ribosomal RNA was removed using a NEBNext rRNA Depletion Kit for bacteria. Libraries from ribo-depleted samples were constructed using the NEB Ultra Directional RNA library prep kit for Illumina. Briefly, 10–500 ng total RNA was subjected to ribosomal RNA depletion and rRNA-free samples were fragmented based on their RNA integrity number. After cDNA synthesis, Illumina-compatible adapters were ligated onto the inserts and the final library quality was evaluated using TapeStation (Agilent Technologies). Libraries were normalized using quantitative PCR and then sequenced on Illumina's NovaSeq 6000 platform using 2 × 150 bp read configuration.

High-quality sequence reads were mapped to the NCBI reference genomes of *E. lenta* strain DSM2243 (GCF_000024265.1) and *H. filiformis* strain AF24-29 (GCF_003459085.1), accordingly. The reads were mapped to the respective reference genomes using Bowtie2 v2.4.5 and sorted with Samtools v1.6 using default parameters^{70,71}. All sequence data were deposited to the NCBI Sequence Read Archive database under the Bioproject ID PRJNA1012298. Read counts were generated using featureCounts v2.0.1 with the flags -p, -B and -C⁷². Gene expression

was quantified as the total number of reads uniquely aligning to the respective reference genomes, binned by annotated gene coordinates.

Differential gene expression and related quality-control analyses were determined using the Bioconductor package DESeq2 in R^{73,74}. Normalization of raw read counts was performed by a scaling method implemented within the DESeq2 package, which accounts for differences in library size and library composition. Reads were also normalized for batch effects where applicable by ComBat-seq⁷⁵. A log₂ fold change shrinkage was performed using the *apeglm* method in DESeq2 (ref. 76). Differential expression of pairwise comparisons (of the different conditions) was assessed using the negative binomial test with a Benjamini–Hochberg false discovery rate adjustment applied for multiple testing corrections.

Proteomics mass spectrometry

Samples for proteomic analysis were prepped using a modified version of the filter-aided sample preparation procedure. A portion of thawed cell pellet was mixed with 500 µl 1× SDS buffer (40 ml of 1× contained 4 g glycerol, 0.67 g Tris–HCl, 0.68 g Tris base, 0.8 g SDS and 6 mg EDTA) and dithiothreitol to 20 mM. The mixture was sonicated at 20% pulsing 2 s on and 2 s off for 5 min. This mixture was then heated at 95 °C for 20 min, followed by 37 °C for 30 min. Iodoacetamide was added to 60 mM, and the mixture was incubated in the dark for 60 min, before dithiothreitol was again added to 60 mM. This prepared lysate was then mixed 1:8 (25 µl:200 µl) with exchange buffer (8 M urea, 0.2% (w/v) deoxycholate, 1 M ammonium bicarbonate, pH 8) and dispensed to a filter unit. The mixture was spun at 14,000 × *g* for 10 min, discarding the filtrate. The filter unit was washed 3 times, each with 200 µl exchange buffer, and spun at 14,000 × *g* for 10 min, discarding the filtrate. The filter unit was then washed twice with 200 µl digestion buffer (0.2% (w/v) deoxycholate, 50 mM ammonium bicarbonate, pH 8) and spun at 14,000 × *g* for 10 min, discarding the filtrate. The filter unit was transferred to a passive collection tube and 100 µl digestion buffer plus trypsin (–1:50 trypsin:protein) and incubated at 37 °C overnight. The following day, the tube was centrifuged at 14,000 × *g* for 10 min, but the filtrate was not discarded. Peptide recovery buffer (50 µl; 50 mM ammonium bicarbonate, pH 8) was added to the filter unit and spun at 14,000 × *g* for 10 min, and this was repeated once more. The resulting three filtrates were transferred to a LoBind tube. To the filtrate, 900 µl of ethyl acetate and 2.5 µl of trifluoroacetic acid were added and vortexed. The mixture was sonicated (10 s at 10%) and centrifuged at 16,000 × *g* for 10 min. The upper organic layer was removed and discarded, taking care not to disturb the phase boundary. The addition of ethyl acetate, sonication, centrifugation and layer removal were repeated twice more, but without the addition of trifluoroacetic acid. Sample tubes were heated uncovered to 60 °C for 5 min to evaporate residual ethyl acetate, then frozen at –80 °C until analysis.

Samples of trypsin-digested proteins were analysed using a Synapt G2-Si ion mobility mass spectrometer that was equipped with a nanoelectrospray ionization source (Waters). The mass spectrometer was connected in line with an Acquity M-class ultra-performance liquid chromatography system that was equipped with trapping (Symmetry C18, inner diameter: 180 µm, length: 20 mm, particle size: 5 µm) and analytical (HSS T3, inner diameter: 75 µm, length: 250 mm, particle size: 1.8 µm) columns (Waters). The mobile-phase solvents were water and acetonitrile, both of which contained 0.1% (volume/volume) formic acid. Data-independent, ion-mobility-enabled, high-definition mass spectra and tandem mass spectra were acquired in the positive-ion mode^{77–80}.

Data acquisition was controlled using MassLynx software (version 4.1), and tryptic peptide identification and relative quantification using a label-free approach were performed using Progenesis Q1 for Proteomics software (version 4.0, Waters)⁸¹. Data were searched against the *E. lenta* protein database to identify tryptic peptides⁸².

Recombinant reductase production and purification

Hexa-histidine-tagged reductase constructs were expressed in *E. coli* Rosetta cells using either the pET28a or pMCSG53 expression vectors, as previously described⁸³. Briefly, expression was performed using 500 ml cultures of Luria–Bertani broth (BD, Miller 244610) plus 100 µM riboflavin, grown to an OD of 0.7–1.0 at 37 °C, then induced with 1 mM β-D-1-thiogalactopyranoside overnight at 20 °C. Kanamycin (30 mg ml^{–1}, pET28a vector) or carbenicillin (100 mg ml^{–1}, pMCSG53 vector) was used for selection. Cultures were pelleted, resuspended in lysis buffer (50 mM Tris–HCl, 300 mM NaCl, 1 mM dithiothreitol, 10 mM imidazole, pH 7.5) and incubated with 500 µg ml^{–1} lysozyme on ice for 30 min. Cells were ruptured by sonication (Branson Digital Sonifier SFX 250) with 40 15 s pulses between 40 s waits. Insoluble material was removed by centrifugation. Resulting supernatants were mixed with Ni-charged resin beads (Bio-Rad Profinity IMAC) to purify the His-tagged reductases. Beads were washed using lysis buffer, and bound protein was eluted using lysis buffer containing an additional 500 mM imidazole. The eluted protein was dialyzed (Slide-A-Lyzer MINI Dialysis Device, 7,000 Da molecular weight cut-off) into 50 mM HEPES and 100 mM NaCl, pH 7.0, for subsequent assays.

Recombinant reductase assay

Assays were performed in an anaerobic chamber under an atmosphere of 2–5% H₂, 2–5% CO₂ and balance nitrogen. Potential electron acceptors were dried in 96-well plates (Falcon 96-well polystyrene microplates 351172) to allow for a 1 mM final concentration at a 200 µl reaction volume. The reaction buffer consisted of a base buffer of 50 mM HEPES and 100 mM NaCl, pH 7.0, which was autoclaved then immediately sparged with nitrogen and was placed into the anaerobic chamber. Powders of methyl viologen (CAS no. 75365-73-0), sodium dithionite (CAS no. 7775-14-6) and flavin adenine dinucleotide (CAS no. 146-14-5) were weighted out and placed into the anaerobic chamber 24 h before use. All components (plastics, buffers and so on) were placed in the anaerobic chamber for at least 24 h before assay use. The powders were resuspended in the base buffer immediately before usage. Methyl viologen was resuspended to 50 mM, sodium dithionite to 25 mM and flavin adenine dinucleotide to 1 mM. The working master mix consisted of 40 µM flavin adenine dinucleotide, 100 µM methyl viologen, and 100 µM sodium dithionite, which yields a deep purple colour. Purified reductases were added to a final concentration of 5 µg per well, and the resulting mixture was multichannel pipetted into the electron-acceptor-containing plates. Assays of CirA, CirC, CirD, CrdD and their point mutants used reductases at 0.5, 15, 5 and 0.5 µg per well, respectively. Resuspension of the dried electron acceptor molecules begins the reaction. The plates were adhesive sealed and read in a BioTek Epoch 2 at OD₆₀₀ for 2 h, where a reduction in absorbance indicates a consumption of methyl viologen as an electron donor in the reaction.

Reductase phylogenetics

Genomes for *E. lenta*, *S. wadsworthensis* and *H. filiformis* were downloaded using ncbi-genome-download (<https://github.com/kbclin/ncbi-genome-download>; see Supplementary Table 14 for genome accessions). We then used *anvi'o* v7.1 to convert genome FASTA files into contig databases (<https://anvio.org/m/contigs-db>) using the contig workflow (<https://doi.org/10.1186/s13059-020-02195-w>), during which Prodigal v2.6.3 identified open reading frames (contigs workflow)^{54,84}. Next, we used the EcoPhylo workflow implemented in *anvi'o* (<https://anvio.org/m/ecophylo>) in ‘tree-mode’ to recover reductase genes in genomes using the Pfam model PF00890 and to explain their phylogeny. Briefly, the EcoPhylo workflow (1) used the program *hmmsearch* in HMMER v3.3.2 (ref. 85) to identify reductases, (2) removed hits that had less than 80% model coverage to minimize the likelihood of false positives due to partial hits, (3) dereplicated resulting sequences using *MMseqs2* 13.45111 (ref. 86) to avoid redundancy, (4) calculated

a multiple sequence alignment with MUSCLE v3.8.1551 (ref. 87) and trimmed the alignment by removing columns of the alignment with trimal v1.4.rev15 (with the parameters ‘-gappyout’)⁵⁹, (5) removed sequences that have more than 50% gaps using the anvio program anvio-script-reformat-fasta, (6) calculated a phylogenetic tree with the final alignment with IQ-TREE 2.2.0-beta COVID-edition⁸⁸ (with the parameters ‘-nt AUTO -m WAG -B 1000’) that resulted in a NEWICK formatted tree file and finally (7) visualized the tree in the anvio interactive interface.

Reductase active-site conservation analyses

AlphaFold models of CirA, CirC, CirD and CrdD were downloaded from Uniprot⁸⁹. Active-site amino acids were identified by independently superimposing N- and C-terminal domains of AlphaFold models to the substrate-bound urocanate reductase crystal structure (PDB code 6T87) using PyMOL v2.5.1 (<http://www.pymol.org/pymol>) ‘align’³⁹. Next, sequences in the monophyletic clade surrounding the experimentally validated sequences were subsetted from the reductase multiple sequence alignment using the program anvio-script-reformat-fasta and alignment positions were sliced in Jalview v2.11.2.5⁹⁰. Finally, the extent of conservancy among the active-site-associated residues was visualized with WebLogo 3 (<https://weblogo.threepplusone.com/create.cgi>).

Statistics and reproducibility

Statistical methods were not used to predetermine sample size. Due to the impracticality of experiment blinding, experiments were not randomized and the investigators were not blinded. However, quantitative metrics were used to measure all results, reducing the risk of bias. Data distribution was assumed to be normal, but this was not formally tested.

Reporting summary

Further information on research design is available in the Nature Portfolio Reporting Summary linked to this article.

Data availability

The datasets generated in our study are available within the paper and Supplementary Information. Quantitative metabolomic raw data files can be found on the MassIVE repository (ID [MSV000093291](https://massive.ucsf.edu/MSV000093291)). Transcriptomic datasets generated in this study can be found under BioProject [PRJNA1012298](https://ncbi.nlm.nih.gov/bioproject/PRJNA1012298). Metagenomic data used in this study are publicly available on NCBI under BioProject IDs [PRJNA912122](https://ncbi.nlm.nih.gov/bioproject/PRJNA912122) and [PRJNA838648](https://ncbi.nlm.nih.gov/bioproject/PRJNA838648). Proteomic datasets can be accessed at <https://doi.org/10.7910/DVN/OY9MPE>. NCBI accession codes for studied proteins are provided in Supplementary Table 10. Source data are provided with this paper.

References

- Moodie, A. D. & Ingledew, W. J. Microbial anaerobic respiration. *Adv. Microb. Physiol.* **31**, 225–269 (1990).
- Gibson, G. R., Macfarlane, G. T. & Cummings, J. H. Occurrence of sulphate-reducing bacteria in human faeces and the relationship of dissimilatory sulphate reduction to methanogenesis in the large gut. *J. Appl. Bacteriol.* **65**, 103–111 (1988).
- Smith, N. W. et al. Hydrogen cross-feeders of the human gastrointestinal tract. *Gut Microbes* **10**, 270–288 (2019).
- Butler, N. L. et al. *Bacteroides fragilis* maintains concurrent capability for anaerobic and nanaerobic respiration. *J. Bacteriol.* **205**, e0038922 (2023).
- Schubert, C. & Udden, G. C₄-dicarboxylates as growth substrates and signaling molecules for commensal and pathogenic enteric bacteria in mammalian intestine. *J. Bacteriol.* **204**, e0054521 (2022).
- Winter, S. E. et al. Gut inflammation provides a respiratory electron acceptor for *Salmonella*. *Nature* **467**, 426–429 (2010).
- Winter, S. E. et al. Host-derived nitrate boosts growth of *E. coli* in the inflamed gut. *Science* **339**, 708–711 (2013).
- Miller, B. M. et al. Anaerobic respiration of NOX1-derived hydrogen peroxide licenses bacterial growth at the colonic surface. *Cell Host Microbe* **28**, 789–797.e5 (2020).
- Rekdal, V. M. et al. A widely distributed metalloenzyme class enables gut microbial metabolism of host- and diet-derived catechols. *eLife* **9**, e50845 (2020).
- Ravcheev, D. A. & Thiele, I. Systematic genomic analysis reveals the complementary aerobic and anaerobic respiration capacities of the human gut microbiota. *Front. Microbiol.* **5**, 674 (2014).
- Bilous, P. T., Cole, S. T., Anderson, W. F. & Weiner, J. H. Nucleotide sequence of the dmsABC operon encoding the anaerobic dimethylsulphoxide reductase of *Escherichia coli*. *Mol. Microbiol.* **2**, 785–795 (1988).
- Silvestro, A., Pommier, J., Pascal, M. C. & Giordano, G. The inducible trimethylamine N-oxide reductase of *Escherichia coli* K12: its localization and inducers. *Biochim. Biophys. Acta* **999**, 208–216 (1989).
- Heinzinger, N. K. et al. Sequence analysis of the phs operon in *Salmonella typhimurium* and the contribution of thiosulfate reduction to anaerobic energy metabolism. *J. Bacteriol.* **177**, 2813–2820 (1995).
- Hensel, M. et al. The genetic basis of tetrathionate respiration in *Salmonella typhimurium*. *Mol. Microbiol.* **32**, 275–287 (1999).
- Cruz-García, C. et al. Respiratory nitrate ammonification by *Shewanella oneidensis* MR-1. *J. Bacteriol.* **189**, 656–662 (2007).
- Krafft, T. et al. Cloning and nucleotide sequence of the psrA gene of *Wolinella succinogenes* polysulphide reductase. *Eur. J. Biochem.* **206**, 503–510 (1992).
- Saltikov, C. W. & Newman, D. K. Genetic identification of a respiratory arsenate reductase. *Proc. Natl Acad. Sci. USA* **100**, 10983–10988 (2003).
- Krafft, T. et al. Cloning and sequencing of the genes encoding the periplasmic-cytochrome B-containing selenate reductase of *Thauera selenatis*. *DNA Seq.* **10**, 365–377 (2000).
- Bender, K. S. et al. Identification, characterization, and classification of genes encoding perchlorate reductase. *J. Bacteriol.* **187**, 5090–5096 (2005).
- McPherson, M. J. et al. Respiratory nitrate reductase of *Escherichia coli*. Sequence identification of the large subunit gene. *FEBS Lett.* **177**, 260–264 (1984).
- Lledó, B. et al. Respiratory nitrate reductase from haloarchaeon *Haloferax mediterranei*: biochemical and genetic analysis. *Biochim. Biophys. Acta* **1674**, 50–59 (2004).
- Yamazaki, C. et al. A novel dimethylsulfoxide reductase family of molybdenum enzyme, Idr, is involved in iodate respiration by *Pseudomonas* sp. SCT. *Environ. Microbiol.* **22**, 2196–2212 (2020).
- Cole, S. T. Nucleotide sequence coding for the flavoprotein subunit of the fumarate reductase of *Escherichia coli*. *Eur. J. Biochem.* **122**, 479–484 (1982).
- Light, S. H. et al. Extracellular electron transfer powers flavinylated extracellular reductases in Gram-positive bacteria. *Proc. Natl Acad. Sci. USA* **116**, 26892–26899 (2019).
- Bogachev, A. et al. Urocanate reductase: identification of a novel anaerobic respiratory pathway in *Shewanella oneidensis* MR-1. *Mol. Microbiol.* **86**, 1452–1463 (2012).
- Speich, N. et al. Adenylylsulphate reductase from the sulphate-reducing archaeon *Archaeoglobus fulgidus*: cloning and characterization of the genes and comparison of the enzyme with other iron-sulphur flavoproteins. *Microbiology* **140**, 1273–1284 (1994).
- Méheust, R. et al. Post-translational flavinylation is associated with diverse extracytosolic redox functionalities throughout bacterial life. *eLife* **10**, e66878 (2021).
- Mikoulińska, O. et al. Cytochrome c-dependent methacrylate reductase from *Geobacter sulfurreducens* AM-1. *Eur. J. Biochem.* **263**, 346–352 (1999).

29. Jardim-Messeder, D. et al. Fumarate reductase superfamily: a diverse group of enzymes whose evolution is correlated to the establishment of different metabolic pathways. *Mitochondrion* **34**, 56–66 (2017).
30. Le, C. et al. Emerging chemical diversity and potential applications of enzymes in the DMSO reductase superfamily. *Annu. Rev. Biochem.* **91**, 475–504 (2022).
31. Almeida, A. et al. A unified catalog of 204,938 reference genomes from the human gut microbiome. *Nat. Biotechnol.* **39**, 105–114 (2021).
32. Wu, S. et al. GMrepo: a database of curated and consistently annotated human gut metagenomes. *Nucleic Acids Res.* **48**, D545–D553 (2020).
33. Diaz-Gerevini, G. T. et al. Beneficial action of resveratrol: how and why? *Nutrition* **32**, 174–178 (2016).
34. Bentley, R. & Haslam, E. The shikimate pathway—a metabolic tree with many branches. *Crit. Rev. Biochem. Mol. Biol.* **25**, 307–384 (1990).
35. Michelucci, A. et al. Immune-responsive gene 1 protein links metabolism to immunity by catalyzing itaconic acid production. *Proc. Natl Acad. Sci. USA* **110**, 7820–7825 (2013).
36. Dong, X. et al. Genetic manipulation of the human gut bacterium *Eggerthella lenta* reveals a widespread family of transcriptional regulators. *Nat. Commun.* **13**, 7624 (2022).
37. Leys, D. et al. Structure and mechanism of the flavocytochrome c fumarate reductase of *Shewanella putrefaciens* MR-1. *Nat. Struct. Biol.* **6**, 1113–1117 (1999).
38. Pankhurst, K. L. et al. A proton delivery pathway in the soluble fumarate reductase from *Shewanella frigidimarina*. *J. Biol. Chem.* **281**, 20589–20597 (2006).
39. Venskutonytė, R. et al. Structural characterization of the microbial enzyme urocanate reductase mediating imidazole propionate production. *Nat. Commun.* **12**, 1347 (2021).
40. Heidelberg, J. F. et al. Genome sequence of the dissimilatory metal ion-reducing bacterium *Shewanella oneidensis*. *Nat. Biotechnol.* **20**, 1118–1123 (2002).
41. Hau, H. H. & Gralnick, J. A. Ecology and biotechnology of the genus *Shewanella*. *Annu. Rev. Microbiol.* **61**, 237–258 (2007).
42. Ikeda, S. et al. *Shewanella oneidensis* MR-1 as a bacterial platform for electro-biotechnology. *Essays Biochem.* **65**, 355–364 (2021).
43. Koh, A. et al. Microbially produced imidazole propionate impairs insulin signaling through mTORC1. *Cell* **175**, 947–961.e17 (2018).
44. Dodd, D. et al. A gut bacterial pathway metabolizes aromatic amino acids into nine circulating metabolites. *Nature* **551**, 648–652 (2017).
45. Steed, A. L. et al. The microbial metabolite desaminotyrosine protects from influenza through type I interferon. *Science* **357**, 498–502 (2017).
46. Haiser, H. J. et al. Predicting and manipulating cardiac drug inactivation by the human gut bacterium *Eggerthella lenta*. *Science* **341**, 295–298 (2013).
47. Koppel, N. et al. Discovery and characterization of a prevalent human gut bacterial enzyme sufficient for the inactivation of a family of plant toxins. *eLife* **7**, e33953 (2018).
48. Alexander, M. et al. Human gut bacterial metabolism drives Th17 activation and colitis. *Cell Host Microbe* **30**, 17–30.e9 (2022).
49. Bess, E. N. et al. Genetic basis for the cooperative bioactivation of plant lignans by *Eggerthella lenta* and other human gut bacteria. *Nat. Microbiol.* **5**, 56–66 (2020).
50. Maini Rekdal, V. et al. Discovery and inhibition of an interspecies gut bacterial pathway for levodopa metabolism. *Science* **364**, eaau6323 (2019).
51. Sasikaran, J. et al. Bacterial itaconate degradation promotes pathogenicity. *Nat. Chem. Biol.* **10**, 371–377 (2014).
52. Wang, H. et al. An essential bifunctional enzyme in *Mycobacterium tuberculosis* for itaconate dissimilation and leucine catabolism. *Proc. Natl Acad. Sci. USA* **116**, 15907–15913 (2019).
53. Zhang, T., Hasegawa, Y. & Waldor, M. K. A bile metabolite atlas reveals infection-triggered interorgan mediators of intestinal homeostasis and defense. Preprint at *bioRxiv* <https://doi.org/10.1101/2023.03.04.531105> (2023).
54. Hyatt, D. et al. Prodigal: prokaryotic gene recognition and translation initiation site identification. *BMC Bioinformatics* **11**, 119 (2010).
55. Mistry, J. et al. Pfam: the protein families database in 2021. *Nucleic Acids Res* **49**, D412–D419 (2021).
56. Eddy, S. R. Profile hidden Markov models. *Bioinformatics* **14**, 755–763 (1998).
57. Almagro Armenteros, J. J. et al. SignalP 5.0 improves signal peptide predictions using deep neural networks. *Nat. Biotechnol.* **37**, 420–423 (2019).
58. Katoh, K. & Standley, D. M. A simple method to control over-alignment in the MAFFT multiple sequence alignment program. *Bioinformatics* **32**, 1933–1942 (2016).
59. Capella-Gutiérrez, S., Silla-Martínez, J. M. & Gabaldón, T. trimAl: a tool for automated alignment trimming in large-scale phylogenetic analyses. *Bioinformatics* **25**, 1972–1973 (2009).
60. Nguyen, L.-T. et al. IQ-TREE: a fast and effective stochastic algorithm for estimating maximum-likelihood phylogenies. *Mol. Biol. Evol.* **32**, 268–274 (2015).
61. Kalyaanamoorthy, S. et al. ModelFinder: fast model selection for accurate phylogenetic estimates. *Nat. Methods* **14**, 587–589 (2017).
62. Hoang, D. T. et al. UFBoot2: improving the ultrafast bootstrap approximation. *Mol. Biol. Evol.* **35**, 518–522 (2018).
63. Delmont, T. O. & Eren, A. M. Linking pangenomes and metagenomes: the *Prochlorococcus* metapangenome. *PeerJ* **6**, e4320 (2018).
64. Altschul, S. F. et al. Basic local alignment search tool. *J. Mol. Biol.* **215**, 403–410 (1990).
65. García-Villalba, R. et al. Metabolism of different dietary phenolic compounds by the urolithin-producing human-gut bacteria *Gordonibacter urolithinifaciens* and *Ellagibacter isourolithinifaciens*. *Food Funct.* **11**, 7012–7022 (2020).
66. Sumner, L. W. et al. Proposed minimum reporting standards for chemical analysis. *Metabolomics* **3**, 211–221 (2007).
67. Odenwald, M. A. et al. Bifidobacteria metabolize lactulose to optimize gut metabolites and prevent systemic infection in patients with liver disease. *Nat. Microbiol.* <https://doi.org/10.1038/s41564-023-01493-w> (2023).
68. Bolger, A. M., Lohse, M. & Usadel, B. Trimmomatic: a flexible trimmer for Illumina sequence data. *Bioinformatics* **30**, 2114–2120 (2014).
69. Blanco-Miguez, A. et al. Extending and improving metagenomic taxonomic profiling with uncharacterized species using MetaPhlan 4. *Nat. Biotechnol.* **41**, 1633–1644, <https://doi.org/10.1038/s41587-023-01688-w> (2023).
70. Langmead, B. & Salzberg, S. L. Fast gapped-read alignment with Bowtie 2. *Nat. Methods* **9**, 357–359 (2012).
71. Danecek, P. et al. Twelve years of SAMtools and BCFtools. *Gigascience* **10**, giab008 (2021).
72. Liao, Y., Smyth, G. K. & Shi, W. featureCounts: an efficient general purpose program for assigning sequence reads to genomic features. *Bioinformatics* **30**, 923–930 (2014).
73. Love, M. I., Huber, W. & Anders, S. Moderated estimation of fold change and dispersion for RNA-seq data with DESeq2. *Genome Biol.* **15**, 550 (2014).

74. R Core Team R: a language and environment for statistical computing (R Foundation for Statistical Computing, 2016); <https://www.R-project.org/>
75. Zhang, Y., Parmigiani, G. & Johnson, W. E. *ComBat-seq*: batch effect adjustment for RNA-seq count data. *NAR Genom. Bioinform.* **2**, lqaa078 (2020).
76. Zhu, A., Ibrahim, J. G. & Love, M. I. Heavy-tailed prior distributions for sequence count data: removing the noise and preserving large differences. *Bioinformatics* **35**, 2084–2092 (2019).
77. Plumb, R. S. et al. UPLC/MS(E): a new approach for generating molecular fragment information for biomarker structure elucidation. *Rapid Commun. Mass Spectrom.* **20**, 1989–1994 (2006).
78. Shliha, P. V. et al. Effects of traveling wave ion mobility separation on data independent acquisition in proteomics studies. *J. Proteome Res.* **12**, 2323–2339 (2013).
79. Helm, D. et al. Ion mobility tandem mass spectrometry enhances performance of bottom-up proteomics. *Mol. Cell Proteom.* **13**, 3709–3715 (2014).
80. Distler, U. et al. Drift time-specific collision energies enable deep-coverage data-independent acquisition proteomics. *Nat. Methods* **11**, 167–170 (2014).
81. Distler, U. et al. Label-free quantification in ion mobility-enhanced data-independent acquisition proteomics. *Nat. Protoc.* **11**, 795–812 (2016).
82. Sayers, E. W. et al. Database resources of the National Center for Biotechnology Information. *Nucleic Acids Res* **50**, D20–D26 (2022).
83. Rivera-Lugo, R. et al. Distinct energy-coupling factor transporter subunits enable flavin acquisition and extracytosolic trafficking for extracellular electron transfer in *Listeria monocytogenes*. *mBio* **14**, e0308522 (2023).
84. Eren, A. M. et al. Community-led, integrated, reproducible multi-omics with anvio. *Nat. Microbiol.* **6**, 3–6 (2020).
85. Eddy, S. R. Accelerated profile HMM searches. *PLoS Comput. Biol.* **7**, e1002195 (2011).
86. Steinegger, M. & Söding, J. MMseqs2 enables sensitive protein sequence searching for the analysis of massive data sets. *Nat. Biotechnol.* <https://doi.org/10.1038/nbt.3988> (2017).
87. Edgar, R. C. MUSCLE: multiple sequence alignment with high accuracy and high throughput. *Nucleic Acids Res.* **32**, 1792–1797 (2004).
88. Minh, B. Q. et al. IQ-TREE 2: new models and efficient methods for phylogenetic inference in the genomic era. *Mol. Biol. Evol.* **37**, 1530–1534 (2020).
89. Jumper, J. et al. Highly accurate protein structure prediction with AlphaFold. *Nature* **596**, 583–589 (2021).
90. Waterhouse, A. M. et al. Jalview version 2—a multiple sequence alignment editor and analysis workbench. *Bioinformatics* **25**, 1189–1191 (2009).

Acknowledgements

We thank H. Lin and N. P. Dylla for assistance with data analyses and L. Comstock for helpful feedback. We thank the University of Chicago

Animal Resources Center for their assistance with mouse work (RRID: SCR_021806). Research reported in this publication was supported by funding from the National Institutes of Health (T32DK007074 to M.A.O., 1S10OD020062-01 to A.T.I., and K22AI144031 and R35GM146969 to S.H.L.) and the Searle Scholars Program (to S.H.L.).

Author contributions

A.S.L., E.G.P. and S.H.L. conceptualized the project. A.S.L., I.T.Y., P.N.B., J.S., K.S. and D.S. performed the experiments. A.S.L., M.S.S., P.N.B. and S.H.L. analysed the data. A.S.L., I.T.Y., P.N.B., J.S. and K.S. performed growth assays. A.S.L. performed ATP determination assays. A.S.L. and J.S. performed protein expression and purification and reductase activity assays. M.S.S., R.M. and A.M.E. performed bioinformatic analysis, including phylogeny and pangenomes. A.S.L., R.R., R.S. and A.S. performed bioinformatics analysis of transcriptomic data. M.W.M., W.L., D.M., M.M. and A.M.S. performed and analysed mass spectrometry. A.T.I. performed and analysed proteomics data. A.S.L., P.N.B., J.S. and E.W. performed animal experiments and maintenance. M.A.O. provided human faecal samples for analysis. A.S.L. and S.H.L. wrote the paper.

Competing interests

The authors declare no competing interests.

Additional information

Extended data is available for this paper at <https://doi.org/10.1038/s41564-023-01560-2>.

Supplementary information The online version contains supplementary material available at <https://doi.org/10.1038/s41564-023-01560-2>.

Correspondence and requests for materials should be addressed to Samuel H. Light.

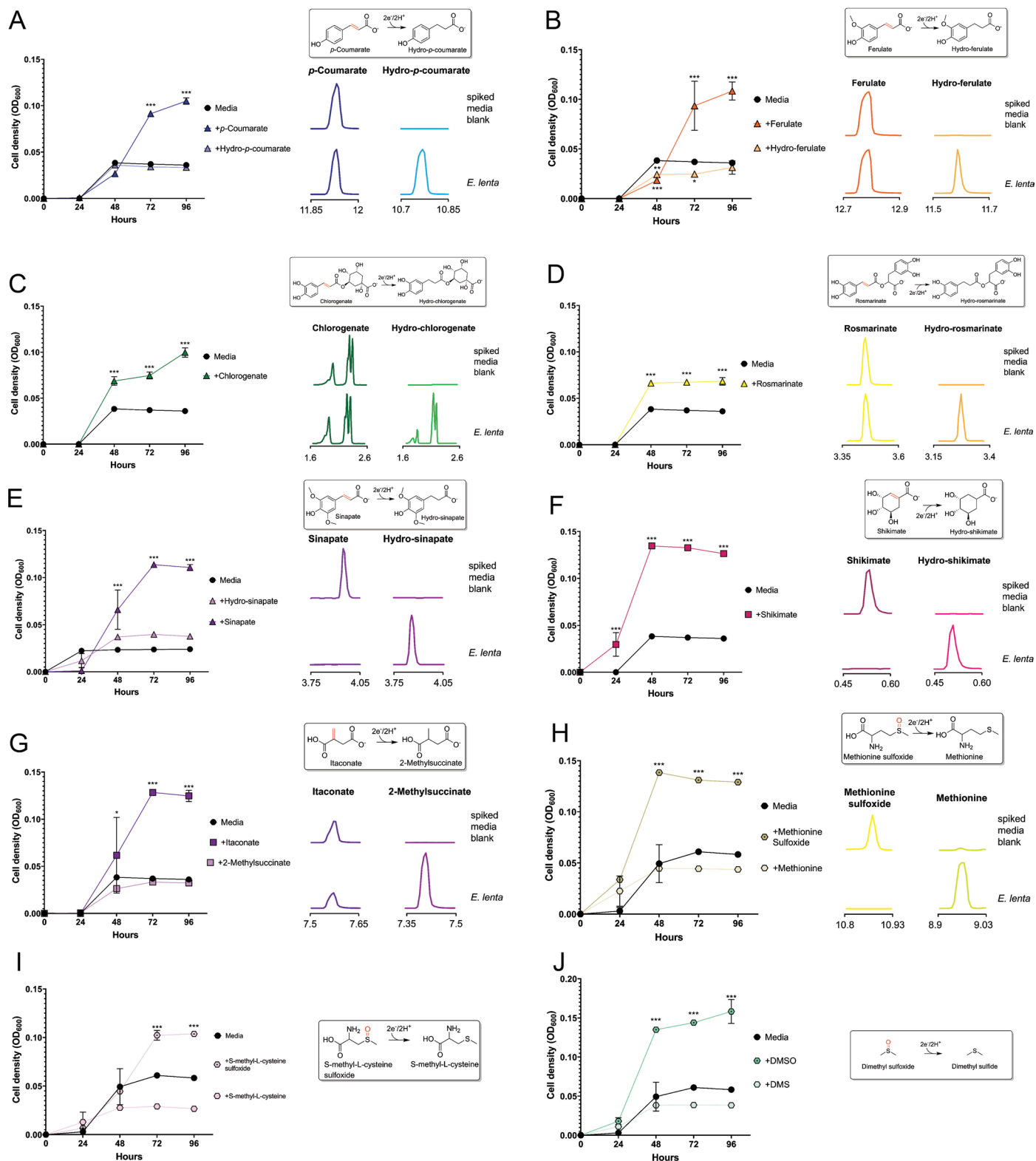
Peer review information *Nature Microbiology* thanks Emily Balskus, Chris Greening and the other, anonymous, reviewer(s) for their contribution to the peer review of this work.

Reprints and permissions information is available at www.nature.com/reprints.

Publisher's note Springer Nature remains neutral with regard to jurisdictional claims in published maps and institutional affiliations.

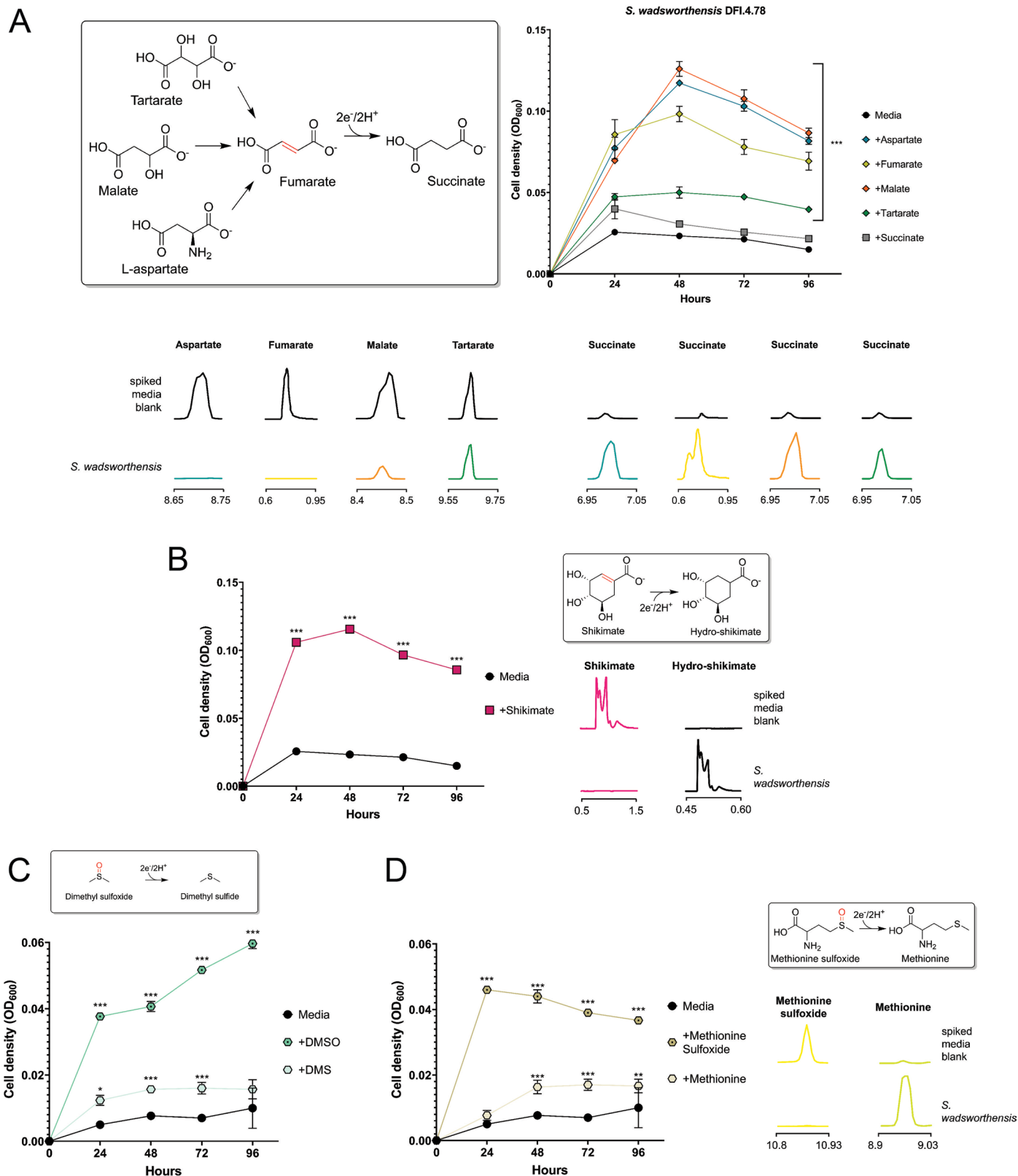
Springer Nature or its licensor (e.g. a society or other partner) holds exclusive rights to this article under a publishing agreement with the author(s) or other rightsholder(s); author self-archiving of the accepted manuscript version of this article is solely governed by the terms of such publishing agreement and applicable law.

© The Author(s), under exclusive licence to Springer Nature Limited 2024



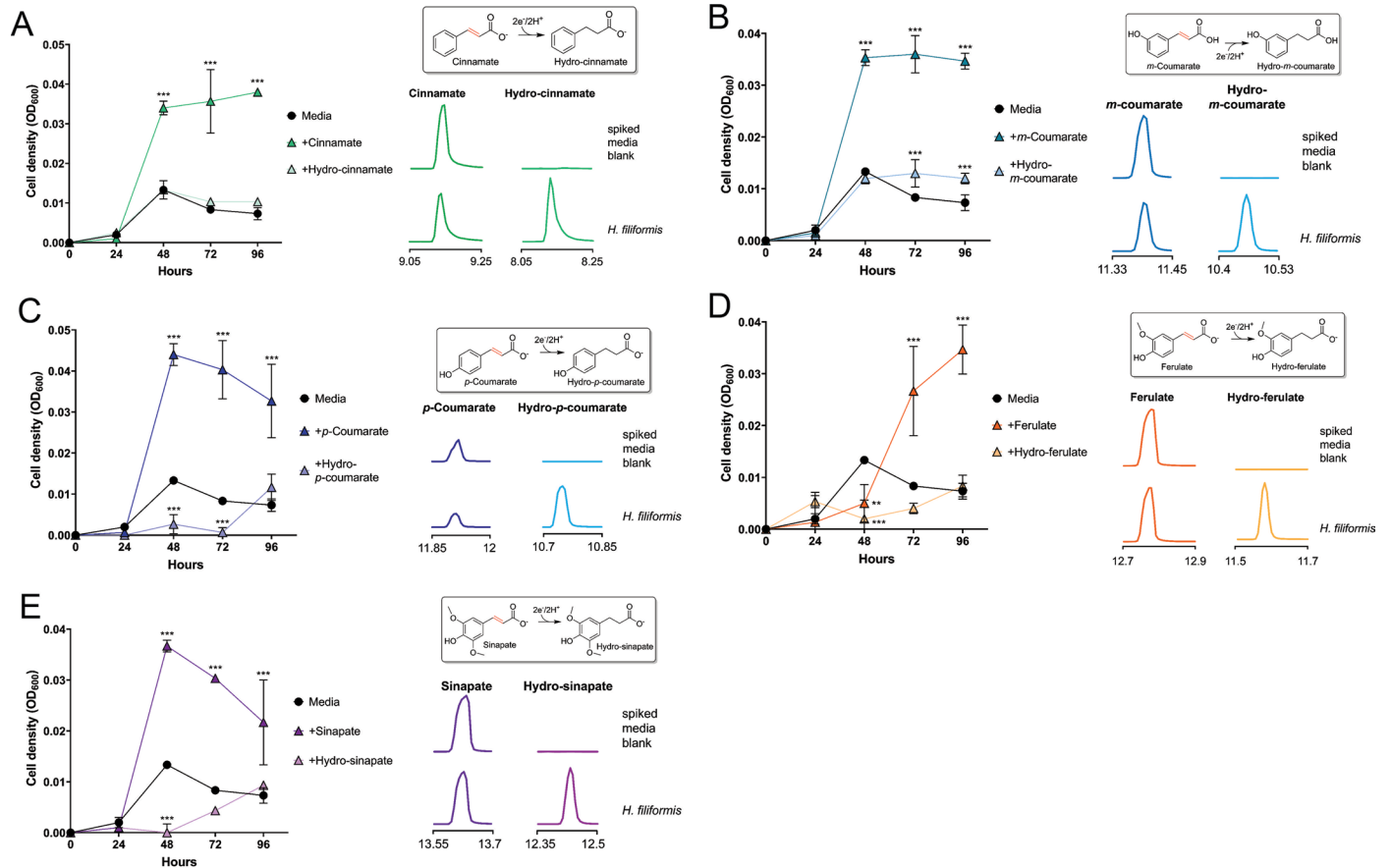
Extended Data Fig. 2 | *E. lenta* uses multiple respiratory electron acceptors. *E. lenta* DSM2243 growth in formate-supplemented media provisioned with electron acceptors: (a) *p*-coumarate, (b) ferulate, (c) chlorogenate, (d) rosmarinatate, (e) sinapate, (f) shikimate, (g) itaconate, (h) methionine sulfoxide, (i) S-methyl-L-cysteine sulfoxide, and (j) dimethyl sulfoxide. A 'no electron acceptor' condition and conditions with predicted reduction products

are included as controls. Extracted ion chromatograms of peaks (matched to available authentic standards) in uninoculated and inoculated growth media. (A)-(D), (G)-(J) were measured by GC-MS; (E), (F) were measured by LC-MS; support for identification of hydro-shikimate in (F) is provided in Supplementary Fig. 5. Data are mean \pm SD ($n = 3$ independent biological replicates). * $p < 0.05$, ** $p < 0.01$, *** $p < 0.001$. Two-way ANOVA, multiple test vs media alone.



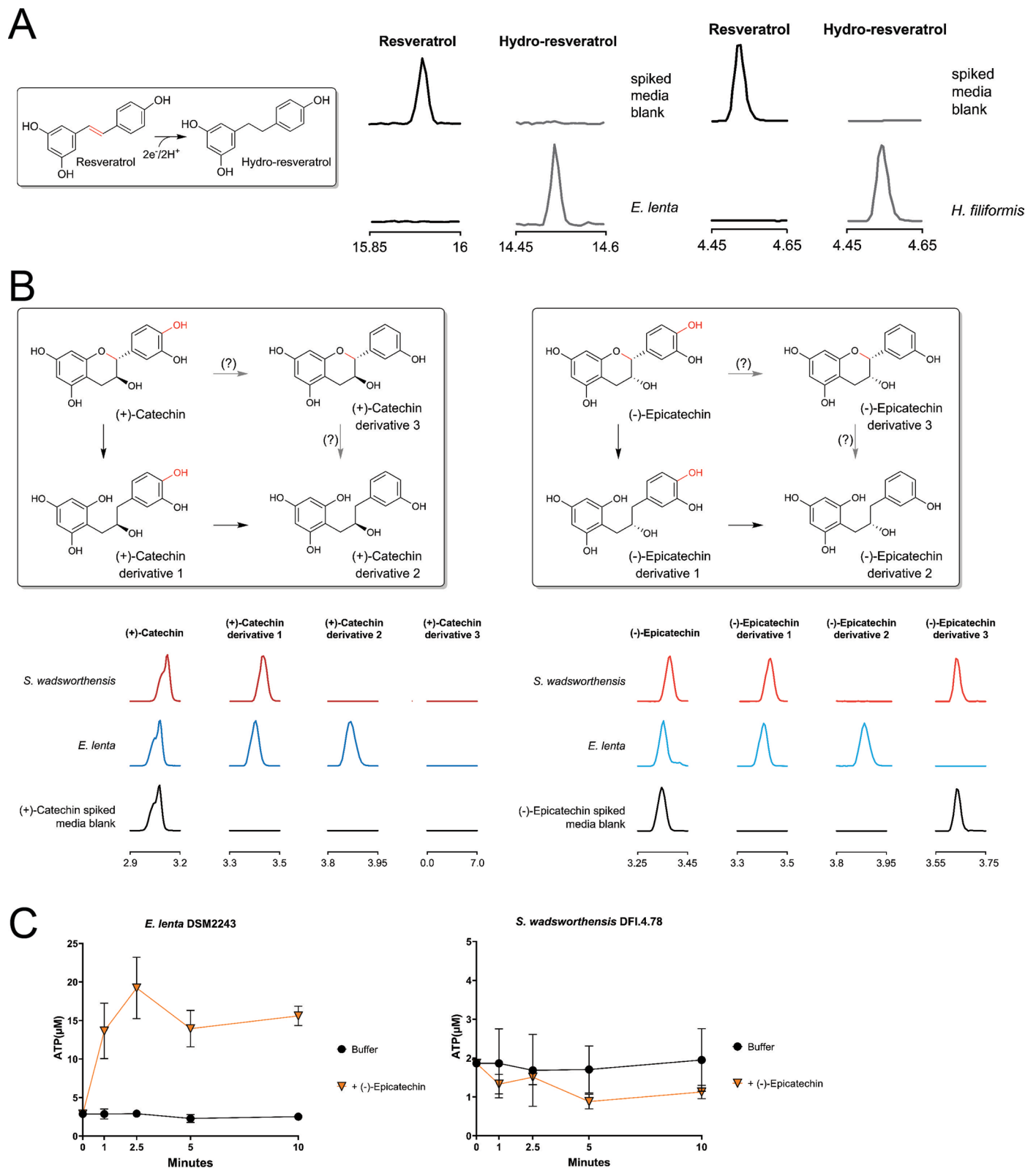
Extended Data Fig. 3 | *S. wadsworthensis* growth-stimulating electron acceptors. *S. wadsworthensis* growth in formate-supplemented media provisioned with electron acceptors: (a) labeled C4-dicarboxylates, (b) shikimate, (c) dimethyl sulfoxide, and (d) methionine sulfoxide. A 'no electron acceptor' condition and conditions with predicted products are included as controls. Extracted ion chromatograms of peaks (matched to

available authentic standards) in uninoculated and inoculated growth media. (A) Fumarate and its succinate reduction were measured by LC-MS, the rest of (A) and (D) were measured by GC-MS; (B) was measured by LC-MS; support for identification of hydro-shikimate in (B) is provided in Supplementary Fig. 5. Data are mean \pm SD ($n = 3$ independent biological replicates). * $p < 0.05$, ** $p < 0.01$, *** $p < 0.001$. Two-way ANOVA, multiple test vs media alone.



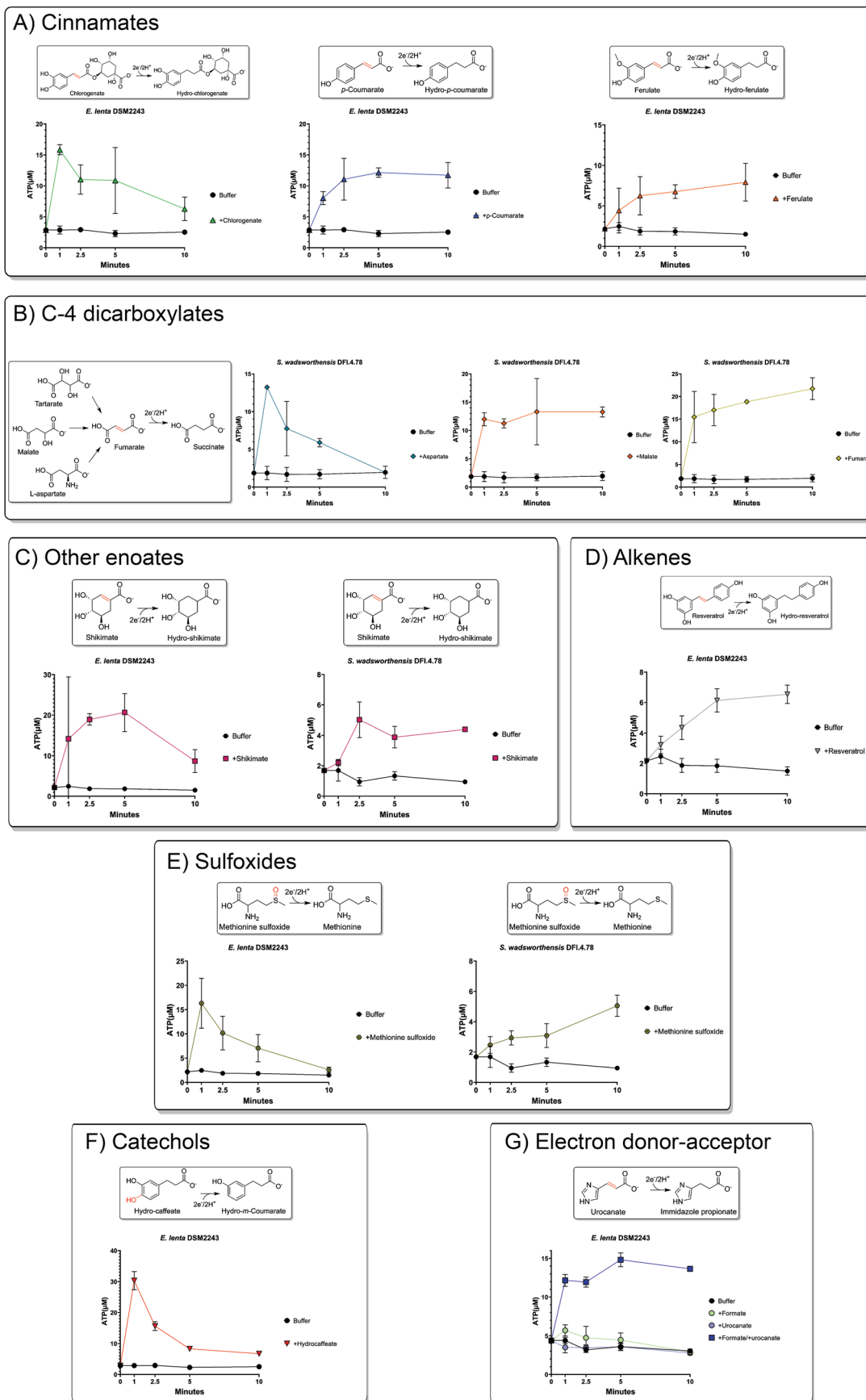
Extended Data Fig. 4 | *H. filiformis* growth-stimulating electron acceptors. *H. filiformis* growth in media provisioned with electron acceptors: (a) cinnamate (b) *m*-coumarate, (c) *p*-coumarate (d) ferulate, and (e) sinapate. A 'no electron acceptor' condition and conditions with predicted products are included as

controls. Extracted ion chromatograms of peaks (matched to available authentic standards) in uninoculated and inoculated growth media. Data are mean \pm SD ($n = 3$ independent biological replicates). * $p < 0.05$, ** $p < 0.01$, *** $p < 0.001$. Two-way ANOVA, multiple test vs media alone.



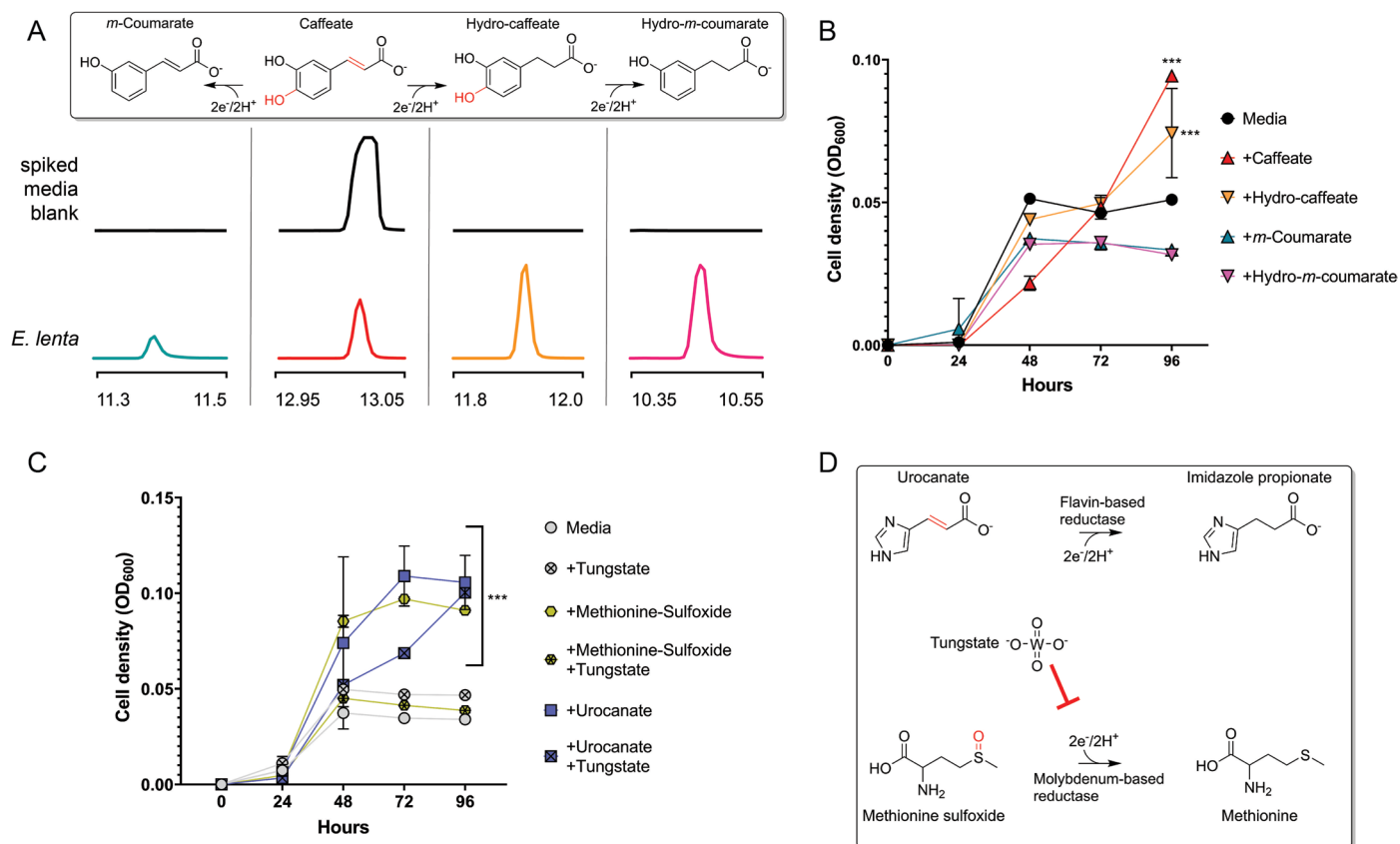
Extended Data Fig. 5 | Electron acceptors not observed to stimulate growth. (a) GC-MS analysis of resveratrol-spiked media before and after *E. lenta* DSM2243 growth and LC-MS analysis of resveratrol-spiked media before and after *H. filiformis* DFI.9.20 growth. The low solubility of resveratrol hindered experiments to assess whether this electron acceptor supported respiratory growth. (b) Potential modification flow for (+)-catechin and (-)-epicatechin, and GC-MS of media spiked with either (+)-catechin or (-)-epicatechin before

and after *E. lenta* DSM2243 or *S. wadsworthensis* DFI.4.78 growth. (c) Resting cell suspensions of *E. lenta* and *S. wadsworthensis* DFI.4.78 in buffer supplemented with 1mM formate assayed cellular ATP concentrations after incubation with buffer alone or (-)-epicatechin, data are mean \pm SD (n = 3 technical replicates). Support for identification of catechin and epicatechin derivatives in (B) is provided in Supplementary Figs. 2 and 3.



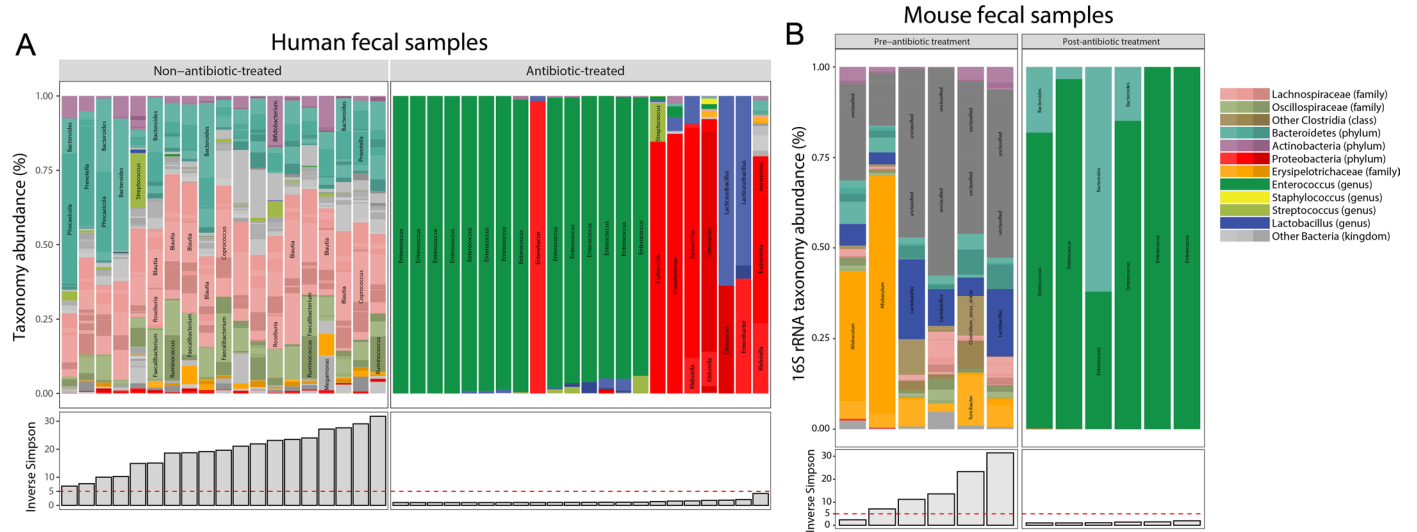
Extended Data Fig. 6 | ATP generation facilitated by electron acceptors. Resting cell suspensions of *E. lenta* and *S. wadsworthensis* in buffer supplemented with 1mM formate assayed cellular ATP concentrations after incubation with different classes of electron acceptors, (a) cinnamates,

(b) C4-dicarboxylates, (c) other enoates, (d) alkenes, (e) sulfoxides, (f) catechols, and (g) electron donor-acceptor combination dependence. Data are mean \pm SD ($n = 3$ technical replicates).



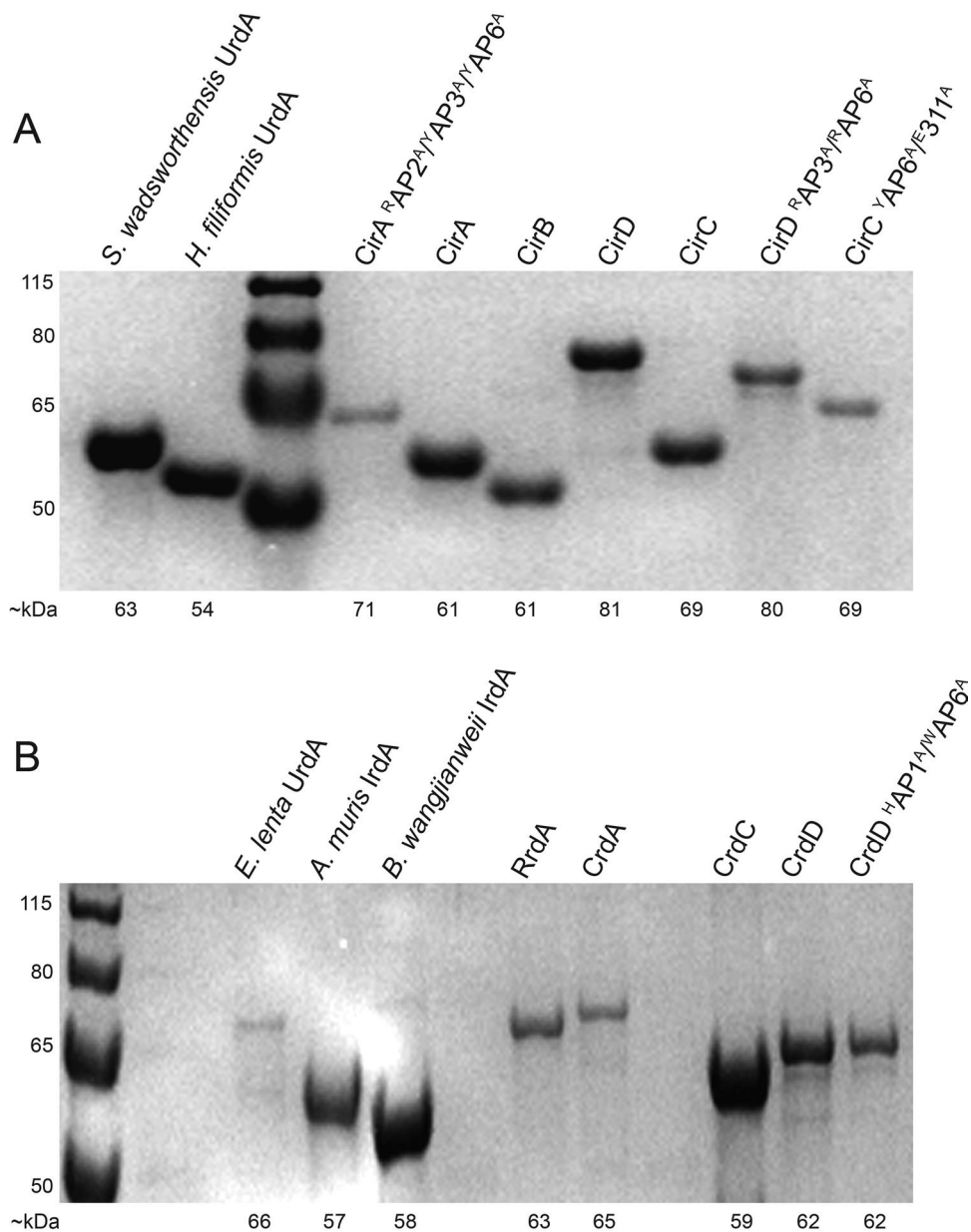
Extended Data Fig. 7 | Caffeate utilization by *E. lenta* and tungstate inhibition of sulfoxide growth enhancement. (a) GC-MS analysis of supernatant collected from *E. lenta* DSM2243 grown in caffeate-spiked media. Extracted ion chromatograms of peaks (matched to authentic standards) in uninoculated and inoculated growth media. Proposed reaction pathways are shown, with peaks for each compound provided beneath its chemical structure. The previously characterized hydrocaffeate dehydroxylase may catalyze the observed dehydroxylation reactions. The observed caffeate reduction to hydrocaffeate provides evidence of a caffeate reductase, while the accumulation of *m*-coumarate suggests that this enzyme may specifically use caffeate. (b) *E. lenta* DSM2243 growth in media supplemented with formate and different cinnamates.

The pattern of cinnamate-dependent growth enhancement supports the conclusions that: (1) dehydroxylation can support respiratory growth and (2) *m*-coumarate is a poor electron acceptor for *E. lenta*. (c) The effect of the molybdopterin reductase inhibitor, tungstate, on *E. lenta* DSM2243 growth. Media was supplemented with formate and the noted electron acceptor, with or without the addition of tungstate. (d) Reactions catalyzed by urocanate and sulfoxide reductases. Tungstate's selective growth inhibition is consistent with sulfoxide, but not urocanate, reduction being catalyzed by a molybdopterin reductase. Data are mean \pm SD ($n = 3$ independent biological replicates). * $p < 0.05$, ** $p < 0.01$, *** $p < 0.001$. Two-way ANOVA, multiple test vs media alone.



Extended Data Fig. 8 | Microbiome composition of fecal samples used for metabolite measurements. (a) Taxonomy abundance in human fecal samples used for metabolomics analyses assessed by shotgun metagenomics.

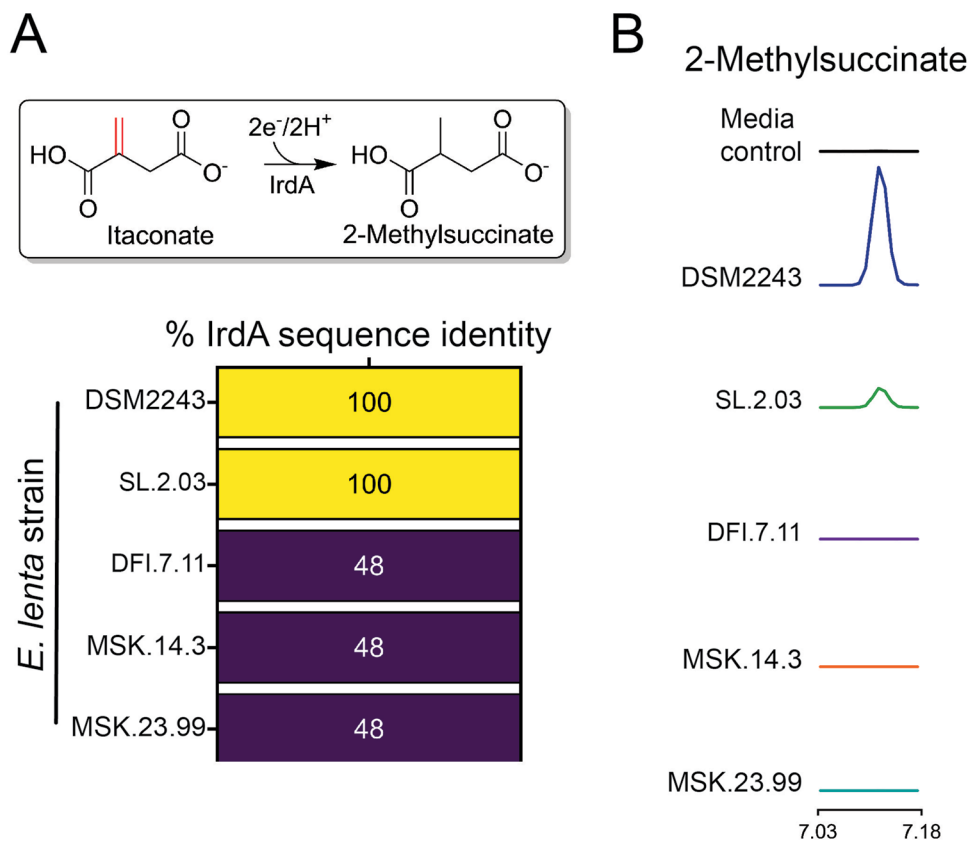
(b) Taxonomy abundance in mouse fecal samples used for metabolomics analyses assessed by 16S rRNA amplicon sequencing. The Inverse Simpson measure of microbiome diversity is also presented.

**Extended Data Fig. 9 | Expression of recombinant reductase enzymes.**

SDS-PAGE gels of reductase enzymes expressed and purified from *E. coli*. **(a)** *H. filiformis* enzymes, except where indicated. **(b)** *E. lenta* enzymes, except where indicated. Proteins run on a 12% acrylamide Bis-Tris gel in a MOPS running buffer,

compared to PageRuler Plus prestained protein ladder (Thermo. #26619).

Expected kDa for both ladder and proteins are labeled. Experiments (A, B) were repeated twice, with similar results.



Extended Data Fig. 10 | Presence of *irdA* predicts itaconate reductase activity of *E. lenta* strains. (a) Schematic diagram of itaconate reduction by IrdA, and sequence identity of the reductase with greatest similarity to IrdA is shown for

indicated *E. lenta* strains strain. (b) Extracted ion chromatograms of authentic standard-matched methylsuccinate peaks from media collected after cultivation with the indicated strain.

Reporting Summary

Nature Portfolio wishes to improve the reproducibility of the work that we publish. This form provides structure for consistency and transparency in reporting. For further information on Nature Portfolio policies, see our [Editorial Policies](#) and the [Editorial Policy Checklist](#).

Statistics

For all statistical analyses, confirm that the following items are present in the figure legend, table legend, main text, or Methods section.

- | n/a | Confirmed |
|-------------------------------------|--|
| <input type="checkbox"/> | <input checked="" type="checkbox"/> The exact sample size (n) for each experimental group/condition, given as a discrete number and unit of measurement |
| <input type="checkbox"/> | <input checked="" type="checkbox"/> A statement on whether measurements were taken from distinct samples or whether the same sample was measured repeatedly |
| <input type="checkbox"/> | <input checked="" type="checkbox"/> The statistical test(s) used AND whether they are one- or two-sided
<i>Only common tests should be described solely by name; describe more complex techniques in the Methods section.</i> |
| <input checked="" type="checkbox"/> | <input type="checkbox"/> A description of all covariates tested |
| <input checked="" type="checkbox"/> | <input type="checkbox"/> A description of any assumptions or corrections, such as tests of normality and adjustment for multiple comparisons |
| <input type="checkbox"/> | <input checked="" type="checkbox"/> A full description of the statistical parameters including central tendency (e.g. means) or other basic estimates (e.g. regression coefficient) AND variation (e.g. standard deviation) or associated estimates of uncertainty (e.g. confidence intervals) |
| <input type="checkbox"/> | <input checked="" type="checkbox"/> For null hypothesis testing, the test statistic (e.g. F , t , r) with confidence intervals, effect sizes, degrees of freedom and P value noted
<i>Give P values as exact values whenever suitable.</i> |
| <input checked="" type="checkbox"/> | <input type="checkbox"/> For Bayesian analysis, information on the choice of priors and Markov chain Monte Carlo settings |
| <input checked="" type="checkbox"/> | <input type="checkbox"/> For hierarchical and complex designs, identification of the appropriate level for tests and full reporting of outcomes |
| <input checked="" type="checkbox"/> | <input type="checkbox"/> Estimates of effect sizes (e.g. Cohen's d , Pearson's r), indicating how they were calculated |

Our web collection on [statistics for biologists](#) contains articles on many of the points above.

Software and code

Policy information about [availability of computer code](#)

Data collection Gen5 3.11 software, used for all plate-reader assays in a BioTek Cytation 5 (growth, enzyme kinetics, colorimetric dehydroxylation). For mass spectrometry culture supernatants were analyzed using a GC-MS (Agilent 7890A GC system, Agilent 5975C MS detector) with an electron impact ionization source, a HP-5MSUI column (30 m x 0.25 mm, 0.25 μ m, Agilent Technologies 19091S-433UI). For RNA-seq libraries were normalized using qPCR and then sequenced on Illumina's NovaSeq 6000 platform. For proteomics samples of trypsin-digested proteins were analyzed using a Synapt G2-Si ion mobility mass spectrometer that was equipped with a nano-electrospray ionization source. For metagenomics analysis of human fecal samples purified DNA was quantified with a Qubit 2.0 fluorometer and sequenced on the Illumina HiSeq platform. For 16S rRNA Library QC was performed using Qubit and TapeStation and sequenced on Illumina MiSeq platform.

Data analysis Data generally was compiled and analyzed in GraphPad Prism 9. For mass spectroscopy of culture supernatant data analyses were performed using MassHunter Quantitative Analysis software (version B.10, Agilent Technologies). For RNA-seq reads were mapped to the respective reference genomes using Bowtie2 v2.4.5 and sorted with Samtools v1.6 using default parameters, and differential gene expression and related quality control analyses were determined using the 773 Bioconductor package DESEQ2 (version 1.36.0) in R. Read counts were generated using featureCounts v2.0.1 with the flags -p, -B, and -C. For proteomic analysis data acquisition was controlled using MassLynx software (version 4.1) and tryptic peptide identification and relative quantification using a label-free approach were performed using Progenesis Q1 for Proteomics software (version 4.0, Waters). For metagenomic analysis of human fecal samples, the human genome was removed by kneaddata and taxonomy was profiled using metaphlan4. For 16S rRNA sequencing Raw V4-V5 16S rRNA gene sequence data is demultiplexed and processed through the dada2 pipeline into Amplicon Sequence Variants (ASVs) with minor modifications in R742 (v4.0.3). Taxonomy of the resultant ASVs were assigned to the genus level using the RDP classifier (v2.13) with a minimum bootstrap confidence score of 80.

For manuscripts utilizing custom algorithms or software that are central to the research but not yet described in published literature, software must be made available to editors and reviewers. We strongly encourage code deposition in a community repository (e.g. GitHub). See the Nature Portfolio [guidelines for submitting code & software](#) for further information.

Data

Policy information about [availability of data](#)

All manuscripts must include a [data availability statement](#). This statement should provide the following information, where applicable:

- Accession codes, unique identifiers, or web links for publicly available datasets
- A description of any restrictions on data availability
- For clinical datasets or third party data, please ensure that the statement adheres to our [policy](#)

The datasets generated within the current study are available within the paper and the supplementary information. Quantitative metabolomic raw data files will be publicly available at the time of publication on MassIVE repository (ID MSV000093291). Transcriptomic datasets generated in this study can be found under Bioproject PRJNA1012298. Metagenomic data used in this study are publicly available on NCBI under BioProject IDs PRJNA912122 and PRJNA838648. Proteomic datasets can be accessed at doi.org/10.7910/DVN/OY9MPE. NCBI accession codes for studied proteins are provided in Supplementary Table 10.

Human research participants

Policy information about [studies involving human research participants and Sex and Gender in Research](#).

Reporting on sex and gender	For human fecal donations we considered neither the sex nor gender of donors.
Population characteristics	For antibiotic treated human fecal donors, inclusion criteria for the study included: age >18 years, ability to provide informed consent (either themselves or by proxy if decisionally incapacitated), and being treated on the hepatology consult service. Detailed population characteristics including age, sex, race, BMI, etiology of liver disease, and several clinical factors impacting liver disease severity can be found in doi.org/10.1038/s41564-023-01493-w .
Recruitment	Fecal samples from healthy, non-antibiotic treated subjects were collected through a prospective fecal collection protocol approved by the institutional review boards at the University of Chicago (UC). All donors provided written and informed consent for IRB-approved biospecimen collection and analysis (UC Protocol IRB20-1384). Inclusion criteria for the antibiotic treated cohort included: age >18 years, ability to provide informed consent (either themselves or by proxy if decisionally incapacitated), and being treated on the hepatology consult service. We attempted to avoid self-selection bias by enrolling a large and reflective population of the patient population within our center. However it is possible that the patient population of this one center may not be reflective of populations at other centers. Additionally some sampling bias may be present as not all enrolled patients produced a sample that could be analyzed and some produced multiple samples.
Ethics oversight	University of Chicago IRB (IRB23-0127)

Note that full information on the approval of the study protocol must also be provided in the manuscript.

Field-specific reporting

Please select the one below that is the best fit for your research. If you are not sure, read the appropriate sections before making your selection.

- Life sciences Behavioural & social sciences Ecological, evolutionary & environmental sciences

For a reference copy of the document with all sections, see nature.com/documents/nr-reporting-summary-flat.pdf

Life sciences study design

All studies must disclose on these points even when the disclosure is negative.

Sample size	No statistical methods were used to predetermine sample sizes. In the majority of experiments a sample size of three was used since this is the minimum number required to perform tests of statistical significance.
Data exclusions	No data were excluded from analysis.
Replication	Experiments were replicated independently three times and the findings were reproducible.
Randomization	Animals were randomly assigned to groups (cages) prior to experimentation.
Blinding	Researchers were not blinded during these experiments, however experimental results were measured using quantitative metrics, reducing the bias risk and making blinding less relevant in this setting.

Reporting for specific materials, systems and methods

We require information from authors about some types of materials, experimental systems and methods used in many studies. Here, indicate whether each material, system or method listed is relevant to your study. If you are not sure if a list item applies to your research, read the appropriate section before selecting a response.

Materials & experimental systems

- | | |
|-------------------------------------|---|
| n/a | Involvement in the study |
| <input checked="" type="checkbox"/> | <input type="checkbox"/> Antibodies |
| <input checked="" type="checkbox"/> | <input type="checkbox"/> Eukaryotic cell lines |
| <input checked="" type="checkbox"/> | <input type="checkbox"/> Palaeontology and archaeology |
| <input type="checkbox"/> | <input checked="" type="checkbox"/> Animals and other organisms |
| <input checked="" type="checkbox"/> | <input type="checkbox"/> Clinical data |
| <input checked="" type="checkbox"/> | <input type="checkbox"/> Dual use research of concern |

Methods

- | | |
|-------------------------------------|---|
| n/a | Involvement in the study |
| <input checked="" type="checkbox"/> | <input type="checkbox"/> ChIP-seq |
| <input checked="" type="checkbox"/> | <input type="checkbox"/> Flow cytometry |
| <input checked="" type="checkbox"/> | <input type="checkbox"/> MRI-based neuroimaging |

Animals and other research organisms

Policy information about [studies involving animals](#); [ARRIVE guidelines](#) recommended for reporting animal research, and [Sex and Gender in Research](#)

- | | |
|-------------------------|--|
| Laboratory animals | Six- to nine-week-old female specific pathogen-free C57BL/6 mice from Jackson Laboratories were used for all experiments. |
| Wild animals | This study did not use wild animals. |
| Reporting on sex | Only female mice were used in this study. |
| Field-collected samples | No field-collected samples were used in this study. |
| Ethics oversight | All mouse experiments were performed in accordance with and approved by the Institutional Animal Care and Use Committee of the University of Chicago under protocol 72599. |

Note that full information on the approval of the study protocol must also be provided in the manuscript.